

JOHANNES GUTENBERG-UNIVERSITÄT
MAINZ

FACHBEREICH PHYSIK, MATHEMATIK UND INFORMATIK


DOCTORAL THESIS

**New applications of nitrogen-vacancy
centers in diamond**

Author:

Till J. LENZ

Supervisor:

Prof. Dr. 

A dissertation submitted for the degree "Doctor of Natural Sciences"

March 9, 2022

Abstract

Magnetometry is widely used in industry, science and everyday life. Applications include navigation, geology, chemical analysis and magnetic resonance imaging (MRI), among many others. The different types of magnetic-field sensors, depending on the application, may differ in sensitivity, bandwidth, operational conditions (e.g. temperature and pressure), spatial resolution and price.

In the last two decades, a new magnetometer type based on nitrogen-vacancy (NV) color centers in diamond has gained a lot of attention. NV magnetometers are not the most sensitive compared to superconducting quantum interference devices (SQUIDs) or atomic magnetometers, but feature remarkable properties such as nanoscale resolutions and the ability to be operated from cryogenic temperatures up to ≈ 700 K and under pressures up to 60 GPa they excel in various applications.

This work presents several applications and advances in sensor development that show the strengths of NV-center-based magnetometry.

In particular, micron sized diamond samples which incorporate a layer with high NV-center density are employed to image vortices in a type-II superconductor using a wide-field configuration.

Furthermore, a setup to image both magnetization of (ferro-)magnetic samples via light polarization and the generated stray magnetic field via NV magnetic imaging is designed and constructed. The functionality was demonstrated on a ferromagnetic thin film that shows stripelike domains upon change of external magnetic field.

In addition to the aforementioned applications, a method to utilize (single-) NV centers at zero field was developed. This was necessary due to failure of conventional NV magnetometry protocols because of line crossings at zero field. With the use of circularly polarized microwave fields, we were able to overcome this issue and extend NV-center magnetometry to applications that require zero-field conditions, such as zero-field nuclear magnetic resonance or observation of the domain structure of magnetic samples across the full hysteresis loop.

Declaration of authorship

Herewith I,

Till J. Lenz

declare that the present thesis, entitled:

“New applications of nitrogen-vacancy centers in diamond”

and the works presented within it are my own. I confirm that:

- This work was done wholly or mainly while in candidature for a research degree at the Johannes Gutenberg University.
- Where any part of this thesis has previously been submitted for a degree or any other qualification at the Johannes Gutenberg University or any other institution, this has been clearly stated.
- Where I have consulted the published work of others, this is always clearly attributed.
- Where I have quoted from the work of others, the source is always given. With the exception of such quotations, this thesis is entirely my own work.
- I have acknowledged all main sources of help.
- Where the thesis is based on work done by myself jointly with others, I have made clear exactly what was done by others and what I have contributed myself.

Mainz, **March 9, 2022**

Signature:

Contents

List of abbreviations	vii
List of Figures	viii
Previously published manuscripts	ix
1 Introduction	1
1.1 Motivation	1
1.2 Nitrogen-vacancy centers in diamond	3
1.2.1 Diamond	3
1.2.2 Structure of the NV center	5
1.2.3 NV-center creation	6
1.2.4 Energy levels of the NV center	7
1.2.5 Ground-state Hamiltonian of the NV center	9
1.3 Magnetometry with NV centers	11
1.3.1 Optically detected magnetic resonance (ODMR)	11
1.3.2 Rabi oscillations	13
1.3.3 Pulsed ODMR	15
1.3.4 Ramsey interferometry	17
2 Wide-field imaging of superconductor vortices with electron spins in diamond	21
2.1 Abstract	21
2.2 Introduction	22
2.3 Experimental setup	22
2.4 Results	23
2.4.1 Optically detected magnetic-resonance images	23
2.4.2 Single-frequency images	25
2.4.3 Pinning	26
2.5 Conclusion	27
2.6 Appendix	28
2.6.1 Methods	28
2.6.2 Acknowledgments	29

3	Imaging Topological Spin Structures Using Light-Polarization and Magnetic Microscopy	31
3.1	Abstract	31
3.2	Introduction	31
3.3	Principles of magneto-optical and wide-field magnetic imaging	34
3.3.1	NV-based magnetic imaging	34
3.3.2	Magneto-optical imaging	36
3.3.3	Combined MOKE/magnetic imaging microscopy	37
3.4	Experimental Methods	37
3.4.1	Magnetic sample	37
3.4.2	Experimental setup	38
3.4.3	Magnetic imaging	42
3.4.4	MOKE imaging	43
3.5	Results	44
3.6	Discussion and Conclusions	47
3.7	Acknowledgements	48
4	Magnetic sensing at zero field with a single nitrogen-vacancy center	49
4.1	Abstract	49
4.2	Introduction	50
4.3	Experimental setup	53
4.4	Results	54
4.4.1	Characterization of the microwave polarization	54
4.4.2	Pulsed optically detected magnetic resonance	56
4.4.3	Ramsey sequence	58
4.5	Other possible approaches to magnetometry with NV centers at zero field	59
4.6	Summary and Outlook	60
4.7	Acknowledgements	61
5	Conclusion and outlook	63
6	Acknowledgements	67
7	Bibliography	70

List of abbreviations

Abbreviation	Description
AOM	Acousto-optic modulator
AWG	Arbitrary waveform generator
BSC	Beam-splitter cube
CCD	Charge-coupled device
CVD	Chemical vapor deposition
CW	Continuous wave
EMCCD	Electron-multiplying charge-coupled device
FFT	Fast Fourier transform
FOV	Field(s) of view
FWHM	Full width at half maximum
HPHT	High pressure, high temperature
ISC	Inter-system crossing
MEG	Magnetoencephalography
MOKE	Magneto-optic Kerr effect
MRI	Magnetic resonance imaging
MW	Microwave(s)
NA	Numerical aperture
NMR	Nuclear magnetic resonance
NV	Nitrogen vacancy (center)
ODMR	Optically-detected magnetic resonance
PCB	Printed circuit board
PD	Photodetector
PID	Proportional-integral-derivative
PL	Photoluminescence
RF	Radio frequency
SC(s)	Superconductor(s)
SNR	Signal-to-noise ratio
SQUID(s)	Superconducting quantum interference device(s)
TEM	Transmission electron microscopy
YBCO	Yttrium barium copper oxide
ZULF	Zero-to-ultra-low field

List of Figures

Introduction

1.2.1 Elementary cell of the diamond lattice	3
1.2.2 Photographs of diamonds with different defect types and concentrations	5
1.2.3 NV center structure for different NV orientations	6
1.2.4 Energy-level diagram of the NV center	9
1.2.5 Detailed Energy-level diagram of the NV center's ground state	11
1.3.6 Cw-ODMR spectra of a single NV center and an ensemble of NV centers	12
1.3.7 Rabi measurement and contrast optimization of a single NV center	14
1.3.8 Pulsed ODMR	17
1.3.9 Ramsey measurement	19

Wide-field imaging of superconductor vortices

2.4.1 Experimental setup and optically-detected magnetic resonance images of superconductor vortices	24
2.4.2 Single frequency images of superconductor vortices in different cooling fields	26
2.4.3 Observation of pinned vortices after removal of the cooling bias field	27

Imaging Topological Spin Structures Using Light-Polarization and Magnetic Microscopy

3.3.1 Nitrogen-vacancy center energy-level diagram and schematic of the polar magneto-optic Kerr effect	36
3.4.2 Experimental setup for light-polarization and magnetic microscopy	40
3.5.3 Magnetization and magnetic field imaging using MOKE and NV-based magnetic field imaging	45

Magnetic sensing at zero field with a single nitrogen-vacancy center

4.2.1 Experimental setup and energy-level diagram of the nitrogen-vacancy center ground state	52
4.4.2 Characterization of the circularity of microwave polarization	55
4.4.3 Optically-detected magnetic resonance spectra as a function of magnetic field for different microwave polarizations	57
4.4.4 Ramsey measurements as a function of magnetic bias field	59

Previously published manuscripts

The following manuscripts have been previously published in peer-reviewed journals and represent the main findings in this doctoral work and will form the core of this thesis:

- [REDACTED]*, **Till Lenz***, [REDACTED]
[REDACTED]
[REDACTED] “Wide-field imaging superconductor vortices with electron spins in diamond”. *Physical Review Applied*, 2018 Sept. 18; **10**, 034032.

*These authors contributed equally to this work

- **Till Lenz**, [REDACTED]
[REDACTED]
[REDACTED]
[REDACTED], “Imaging Topological Spin Structures Using Light-Polarization and Magnetic Microscopy”, *Physical Review Applied*, 2021 Feb. 17; **15**, 024040.

- **Till Lenz**, [REDACTED]
[REDACTED], “Magnetic sensing at zero field with a single nitrogen-vacancy center”, *Quantum Science and Technology*, 2021 Jun15; **6**, 3.

The previously mentioned papers are directly incorporated into chapters [2](#), [3](#), [4](#) of this thesis with only minor editorial changes to fit the thesis format compared to the originally published manuscripts.

The following previously published co-authored manuscripts present minor works in the scope of this thesis. They are partially included or used as references when appropriate.

- [REDACTED], **Till Lenz**, [REDACTED], [REDACTED], "Color Centers in Diamond as Novel Probes of Superconductivity", *Journal of Superconductivity and Novel Magnetism*, 2018 Sep 28; **32**, pages 85–95.
- [REDACTED] **Till Lenz**, [REDACTED], [REDACTED], [REDACTED], "Zero-field magnetometry based on nitrogen-vacancy ensembles in diamond", *Physical Review Applied*, 2019 Jun. 27; **11**, 064068.

Thesis outline

Chapter 1

In the first part of this thesis, a short motivation on nitrogen-vacancy (NV) center based magnetometry is presented and specific advantages and disadvantages with respect to other magnetometers are discussed. In addition, the physics of NV centers is introduced and different magnetometry protocols are presented.

Chapter 2

This chapter presents the application of NV-center magnetometry to study a superconductor. More specifically, low-temperature NV magnetometry in combination with a widefield microscope is used to image vortices in a type-II superconductor for the first time in a widefield configuration.

Chapter 3

Chapter 3 demonstrates the combination of magneto-optic Kerr effect (MOKE) imaging, which is a well established technique for domain-wall imaging, with NV imaging. Both techniques measure different physical quantities and therefore a combination gives rise to a more complete picture of the underlying system. With MOKE one measures the magnetization, while with NV magnetometry the stray magnetic field is determined. The successful combination of both techniques into one setup is demonstrated by the measurement of magnetic domains in a ferromagnetic thin film.

Chapter 4

This chapter discusses the implementation of circularly polarized microwave (MW) fields to extend the application range of NV centers to the regime with zero bias field. The quality of the circularity of the MWs is analyzed, and a sensitivity of $\approx 350 \text{ nT}/\sqrt{\text{Hz}}$ in the absence of any bias fields is estimated.

Chapter 5

The last chapter summarizes the findings during the work for this thesis and presents an outlook for the different applications and techniques.

1 Introduction

1.1 Motivation

Magnetometry is ubiquitous in different industrial and scientific fields, but also in daily life. Applications range from a compass in your smartphone over altitude measurements in aircrafts, (ferrous) metal detection, geology, hard-drive disks and chemical analysis to medical applications such as magnetic-resonance-imaging (MRI) and magnetoencephalography (MEG).

As diverse as the applications of magnetometry, so too are the requirements on the sensors, e.g. their sensitivity, bandwidth, spatial resolution, dynamic range and price, just to name a few. As a result, a large family of different magnetometer types were developed over the years. Some prominent examples of different magnetometer types are Hall probes, superconducting quantum interference devices (SQUIDs), atomic magnetometers, pick-up coils and magnetoresistive sensors.

Even in your phone, you can usually find miniaturized magnetoresistive sensors or Hall probes, since their simplicity, small size and price allows manufacturers to implement them in integrated circuits. By contrast, in nuclear magnetic resonance (NMR), where AC magnetic fields in the MHz to GHz range are detected, pick-up coils are still most commonly used. This already showcases that different magnetometer types have specific applications in which they excel and there is no “one type fits all” sensor.

Nonetheless, the magnetometers achieving the best sensitivities are currently alkali-vapor-cell magnetometers and SQUIDs. Both magnetometer types have achieved sensitivities of $\approx 150 \text{ aT}/\sqrt{\text{Hz}}$ [1, 2]. Due to their extraordinarily high magnetic-field sensitivity, both magnetometer types are well suitable for application in MEG, i.e. detecting the magnetic signals generated by the human brain, or in so-called zero-to-ultra-low-field (ZULF) NMR. In both, ZULF-NMR and MEG the signal amplitude is usually well below 1 pT and at frequencies below 1 kHz [3, 4]. In this frequency regime, inductive detection via a pick-up loop as in conventional NMR is not sensitive enough and atomic and SQUID magnetometers prevail. While both, magnetometers excel in terms of sensitivity, both have very specific environmental requirements, especially regarding the operating temperature. SQUIDs work at cryogenic temperatures up to 77 K [5] and atomic vapor cells usually require temperatures of $\approx 400 \text{ K}$ for optimum sensitivity. A detailed discussion, including that of various types of vapor-cell magnetometers, can be found in the book D. Budker and D. F. Jackson Kimball (eds.): **Optical Magnetometry**; Cambridge University Press, 2013 [6]

In the last two decades, another sensor type based on color centers in diamond emerged

granting access to some regimes and applications in highly sensitive magnetometry that were not accessible before. Specifically, the nitrogen-vacancy (NV) color center in diamond has shown extraordinary characteristics in terms of its combination of high sensitivity, high spatial resolution, and the ability to operate as vector magnetometer as well as its operation in a wide range of environments. For example, NV magnetometry applications have been demonstrated from cryogenic temperatures [7, 8] up to 700 K [9] and even under pressures up to 60 GPa [10].

Spatial resolution, sensitivity and, for example, imaging speed can vary strongly within the family of NV magnetometers. While the highest spatial resolution (below 10 nm) is achieved by using a single NV center, the sensitivity is usually limited to $\approx 50 \text{ nT}/\sqrt{\text{Hz}}$ by photon shot noise [11, 12]. Sensitivities below $1 \text{ nT}/\sqrt{\text{Hz}}$ and down to $\approx 1 \text{ pT}/\sqrt{\text{Hz}}$ [13, 14] are achieved using larger ensembles, with the drawback of a resolution on the order of $100 \mu\text{m}$.

Shallow layers of ensembles of NV centers can be used for widefield magnetic imaging with a resolution on the order of $\approx 500 \text{ nm}$, determined by the optical diffraction limit and area sensitivities of $\approx 1 \mu\text{T}\mu\text{m}/\sqrt{\text{Hz}}$ [15–17].

This versatility of measurement modalities of NV-based magnetometry allows for the study of a plethora of different samples such as superconductors [7, 18], (anti-)ferromagnets [19, 20], neurons [21], etc. Moreover, the simplicity of NV magnetometry allows for a combination of NV magnetic sensing/imaging with already existing powerful techniques, such as magneto-optic Kerr effect (MOKE) imaging.

The main focus of this work is to present new applications and measurement modalities of NV centers in widefield magnetic field imaging, and development of a technique to utilize NV centers as magnetic-field sensors without the need of a potentially unwanted/invasive bias field.

The first observation of vortices in type-II superconductors by widefield magnetic imaging will be discussed. Afterwards, the combination of an imaging system for magnetization and magnetic fields is proven useful to study domain walls in ferromagnetic samples. Last but not least, a technique to extend the dynamic range of the NV to zero ambient magnetic field is shown, which opens the door for a vast range of additional applications.

1.2 Nitrogen-vacancy centers in diamond

Before going into detail about the different applications and methods that were demonstrated during this thesis work. The following section will introduce the basic physics of the nitrogen-vacancy color center in diamond and the magnetometry protocols of relevance to the later presented words.

1.2.1 Diamond

To start off we will resume some basic properties of diamond, the host material of nitrogen-vacancy (NV) centers. Diamond is the hardest naturally occurring material on our planet, with a rating of 10 on the Mohs scale [22]. Furthermore, it is a typically colorless semiconductor with a bandgap of ≈ 5.49 eV and a wide range of applications [23, 24]. Many of the applications are based on the hardness such that diamond can be used for drills, grinding, glass cutting etc. In addition, it is famous for its sparkling appearance due to the high refractive index of ≈ 2.4 [25], which leads to total internal reflection already at relatively large angles of incidence. This, together with a proper cut, leads to the sparkle that we associate with diamonds. Furthermore, diamond consists of carbon atoms that are arranged in a face-centered cubic lattice with an diatomic basis. An elementary cell of diamond is shown in Fig.1.2.1.

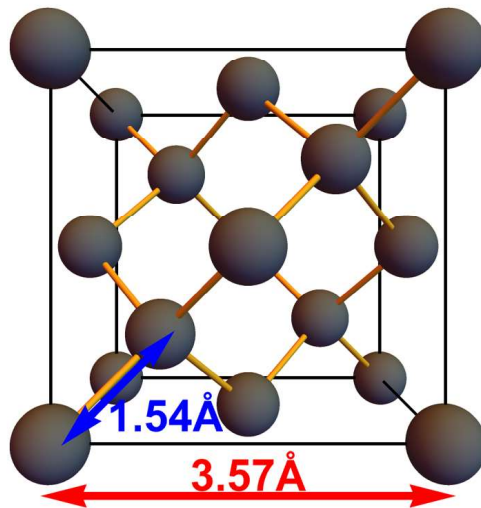


Figure 1.2.1: Schematic of an elementary, cubic cell of the diamond lattice. One can observe that diamond has a face-centered-cubic (fcc) structure with a diatomic basis. Black spheres represent carbon atoms while the yellow tubes indicate atomic bonds.

The unit cubic cell has a lattice constant of 3.57 \AA , while the distance between next neighbours is 1.54 \AA [23]. Carbon itself has many different allotropes, i.e. different structures in which it can appear as a solid at normal conditions. Examples are graphite, graphene, fullerenes, carbon nanotubes and of course diamond. It should be noted here, that under normal conditions diamond is only a metastable allotrope of carbon, while graphite is the stable one. This is the reason why diamond is rare and requires special procedures to be created. Even though it is only metastable at normal conditions, due to a high energy barrier [26] the half life time of the transformation back to graphite is long enough to consider it stable on timescales that are relevant for us humans. In nature, diamond is formed under high pressures of $7 - 8 \text{ GPa}$ and high temperatures of $1400 - 1600^\circ \text{ C}$ [27] within the earth's mantle. Nowadays, it is also possible to produce diamonds synthetically in a (more or less) controlled environment. There are mainly two different techniques for diamond fabrication. One is called the high-pressure, high-temperature (HPHT) method and the another one microwave-assisted chemical-vapour deposition (CVD). The first aims to mimic the conditions in which natural diamonds grow to create diamonds out of graphite. This means that vessels are heated up and put under high pressure, which in turn can lead to relatively high amount of impurities (especially nitrogen) in HPHT diamonds. In contrast to this, CVD diamonds are grown at much lower temperatures around $700 - 1200^\circ \text{ C}$ and pressures in the range of tens of mbars. Here, a seed crystal is needed and with the use of a microwave (MW) plasma, dangling bonds on the diamond surface are created which can then step-by-step incorporate additional carbon atoms to diamond lattice. Typically, methane gas in the growth chamber is used as the carbon source [27]. Both synthesis methods also differ in the quality/purity of the produced diamonds. Even though it is also possible nowadays to create very pure diamonds with boron and nitrogen inclusions below 0.1 ppm via the HPHT method [28], usually HPHT diamonds contain more impurities compared to CVD diamonds [27]. The CVD growth also offers the possibility to isotopically enrich the spin-0 ^{12}C carbon isotope to above 99.999% [29], which results in an effectively magnetic-noise-free lattice. This can be of major importance to achieve better sensitivities (more details below) [30, 31].

Even with these synthesis methods for diamonds, in which the diamond quality is to a large extend controllable, it is not possible to create perfect macroscopic diamonds, which aligns well with the phrase that nature is not perfect. As a result, the crystal lattices of diamonds contain a variety of defects. The different types of crystallographic defects can, in a first step, be distinguished by their dimensionality. There exist zero dimensional point defects, which are strictly located at or around a single lattice site. Examples are: lattice vacancies, interstitial atoms or substituting atoms, e.g. in diamond a nitrogen could replace a carbon

atom. One-dimensional line defects include edge dislocations, where a crystal plane ends within the crystal. Moreover, there are prominent (two-dimensional) planar defects like grain boundaries in polycrystalline materials or stacking faults. Additionally, bulk defects such as inclusion of larger amounts of a different material or pores may occur [32].

1.2.2 Structure of the NV center

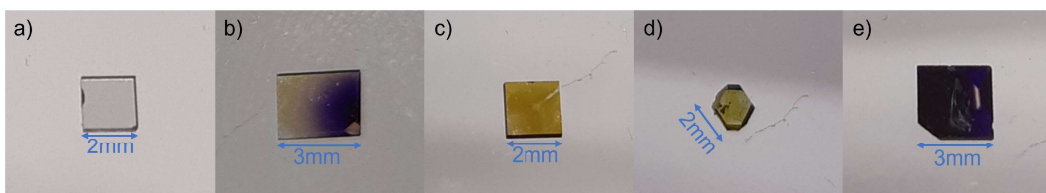


Figure 1.2.2: Photographs of different diamond samples with different defect types and concentrations. a) Sample JGU_NV4, a sample with little to no impurities that is used for single-NV experiments. b) Sample B7, which has a gradient of NV-center density, increasing from left to right. c) Sample W6 contains a large number of nitrogen defects (P1 centers). d) Sample F13, which has a relatively high number of vacancies. e) sample S5 was irradiated with a high dose of electrons, which make the sample appear almost black.

In the following, the spotlight is on a very specific point defect, the nitrogen-vacancy (NV) color center in diamond. Color centers are point defects and obtain their name by their ability to absorb visible light and therefore color otherwise colorless materials (e.g. diamonds). The ability to absorb visible light is traced back to the fact that those defects inherit one or several unpaired electrons, which can be optically excited. In diamond, many different color centers have been observed. For example, diamonds can appear yellow (nitrogen), blue (boron), pink (nitrogen-vacancy), green (vacancy). The name in the brackets indicates the nature of the most prominent color center within accordingly colored diamonds. A collection of diamonds with different types of impurities and different impurity concentrations is shown in Fig. 1.2.2.

The NV center itself, as the name suggests, is composed of a substitutional nitrogen atom and a neighbouring lattice vacancy (see Fig. 1.2.3). NV centers were observed in two charge states: the neutral NV^0 and the negatively charged NV^- , which captures an additional e^- from a donor inside the diamond crystal. The charge state will not be explicitly mentioned further in this thesis and we assume that NV center refers to the NV^- , as the NV^- exhibits the remarkable properties used for applications, that are of importance in this work. Applications are not only limited to magnetometry, but also range from qubits for quantum-information

processing to sensing of temperature, pressure and electric fields [10, 33–37]. More recently, NV centers have also been used to search for exotic (beyond Standard Model) interactions[38–40].

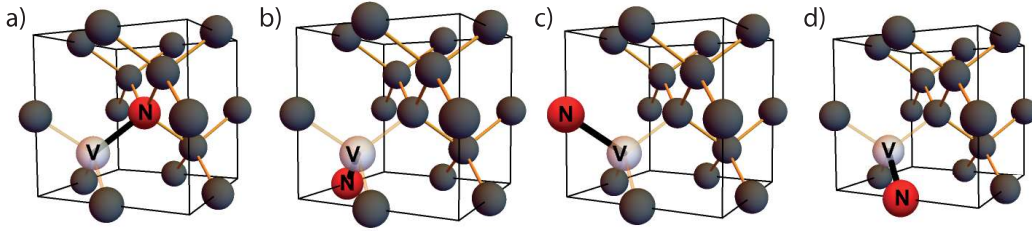


Figure 1.2.3: a), b), c), d) show the structure of the NV center within the diamond lattice for four NV centers aligned along four different axes.

Furthermore, the NV center exhibits a C_{3v} symmetry, which means it has a 3-fold rotational symmetry axis and a mirror plane perpendicular to the symmetry axis. For magnetometry purposes the symmetry axis is of particular interest, because it serves as a natural quantization axis of the system and can be aligned along four different equivalent crystallographic axes. In particular, the axes are $[111]$, $[\bar{1}\bar{1}1]$, $[\bar{1}1\bar{1}]$, $[1\bar{1}\bar{1}]$. Examples are shown in Fig. 1.2.3, while the opposite orientations, i.e. switching the position of the nitrogen atom and the vacancy are also possible and are not distinguishable from the inverted version. This is particularly advantageous for applications, because the different orientations allow for a full reconstruction of the magnetic field vector [41].

1.2.3 NV-center creation

Before moving on to a detailed discussion of the NV-center’s energy levels, this section will provide some basic information on the formation and engineering of NV defects and how their properties can be tailored to different sensing applications.

A common approach, which was also pursued in this work, is to use a high quality CVD diamond with very low number of defects as starting material and artificially create NV centers afterwards. As mentioned earlier, the ingredients for an NV center are a nitrogen atom and a neighbouring lattice vacancy.

Ingredient no. 1, the nitrogen atoms, are mainly inserted into the diamond lattice by two different techniques. The first technique uses a nitrogen-containing ion beam and shoots nitrogen ions with a defined energy into the diamond. The depth from the surface at which the nitrogen ions come to a standstill can be tuned by adjusting the kinetic energy of the ions. A

good estimate for the depth as a function of ion energy can be obtained by “The stopping and range of ions in matter” software [42]. This usually slightly underestimates the actual depth value, as the simulation does not account for channeling effects due to the lattice structure of the diamond [43]. The second technique is called δ -doping. Here, a layer of diamond is grown using the CVD method while nitrogen gas is present in the growth atmosphere. This leads to incorporation of nitrogen in the layers during whose growth nitrogen was present in the growth chamber. Under very specific conditions, this method also allows for the creation of NV ensembles with preferential alignment [44, 45].

Ingredient no. 2, the vacancy, is usually created by some sort of irradiation. Commonly used radiation types are electrons [46, 47], ions (e.g. carbon [48] and helium [49]) and photons [50]. Recently, especially the irradiation with helium ions has gained interest, as it allows for the creation of NV centers with long coherence times [51]. Another effect that is often utilized, is that when nitrogen ions are implanted, they also create vacancies in the lattice while they are slowing down [52].

Now that both ingredients are added to the diamonds, they also need to be combined as they are not necessarily directly next to each other. This is done by a process called annealing. During annealing, the diamond is heated up in a vacuum environment to a temperature of 700 – 1200° C, depending on the exact protocol. At temperatures above 700° C vacancies become mobile, and when they reach a position next to a nitrogen atom they stick there and form the NV center [53]. It is also possible to combine the annealing step with the irradiation step, i.e. constantly annealing the sample during irradiation. This avoids the formation of aggregates of vacancies [54].

Despite optimized protocols for implantation irradiation and annealing, the creation yield of NV centers is only $\approx 50\%$ for high-energy implantations and can reduce to less than 1% for ions with kinetic energies smaller than 10 keV [52]. Further details on the NV center creation can be found in Ref.[55].

1.2.4 Energy levels of the NV center

As mentioned earlier, the high interest in NV centers across different fields of metrology and quantum information is based on its unique energy-level structure. A schematic of the NV center’s energy level structure is shown in Fig. 1.2.4. The electronic system of the NV center is defined by six electrons. Four originate from the non-existent covalent bonds, due to the vacancy, one additional from the nitrogen atom and the sixth one from another donor in the diamond lattice. The six electrons form a spin-1 system as ground state of the NV center. This can be separated into three magnetic sublevels $m_s = 0, \pm 1$ where the number represents

the spin projection along the NV axis. Moreover, there is a spin-1 excited state and two singlet (spin-0) states, which are located in between the triplet states in the energy-level diagram.

The energy difference between the ground and excited triplet (spin-1) states corresponds to a wavelength of 637 nm (zero-phonon line) [56], while the energy difference between the two singlet states corresponds to 1042 nm [57]. The incorporation of the NV center into the diamond lattice also leads to a coupling of the NV to phonons. This results in phonon sidebands in the absorption and emission spectra of the NV centers [58]. In particular, the emission spectrum is mostly red shifted, i.e. creating a photon and phonon(s) during deexcitation from the excited state, and the absorption is mostly blue shifted, i.e. creating phonons in addition to the electronic excitation of the NV center. This allows for excitation of the NV center with green light (in this work 515 or 532 nm) and fluorescence detection in the range of 650-800 nm. Moreover, the energy-level structure and spin-dependent decay rates allow for efficient polarization of $\approx 80\%$ into the $m_s = 0$ state under illumination with green light [34].

Transitions between the triplet and singlet manifolds occur non-radiatively with much lower transition rates than between states of equal multiplicity [59].

This mechanism leading to the polarization is based on the fact that optical transitions are spin conserving and that the probability of a (non-radiative) intersystem crossing (ISC) between the excited triplet state to the excited singlet state is spin-dependent. I.e. the probability of the $m_s = \pm 1$ states to undergo the ISC is higher than of the $m_s = 0$ state. During the second ISC the transition rates from the lower singlet state to all three m_s sublevels are similar, which results after repetitive cycling through the singlet states in a high degree of spin polarization in the $m_s = 0$ state. Moreover, the fact that the decay channel via the singlet states is much slower than a direct decay via emission of a red photon allows for optical readout of the spin state. This is mainly because the ISC is an electric dipole forbidden transition and therefore the decay rate much slower than for decays within a singlet/triplet manifold. Together with the fact that the $m_s = \pm 1$ states have a higher probability of undergoing the slow decay via the singlet states, this leads to a fluorescence reduction of about 30% for NVs in the $m_s = \pm 1$ states compared to those in the $m_s = 0$ state.

To summarize, it is possible to optically initialize (polarize) the NV-center's spin and additionally read out the spin state optically. Of high importance for magnetometry is the spin-1 ground state. Here, the $m_s = \pm 1$ states are lifted from the $m_s = 0$ state due to spin-spin interactions, with an energy difference D corresponding to a frequency of 2.87 GHz ($E = hf$) as indicated in the inset of Fig. 1.2.4 [56]. Moreover the $m_s = \pm 1$ sublevels are subjected to the Zeeman effect and the separation $\Delta\nu$ between them corresponds to $\Delta\nu = 2\gamma_{\text{NV}}B_{\text{NV}}$, with $\gamma_{\text{NV}} = 2.8\text{ MHz/G}$ being the gyromagnetic ratio of the electron and B_{NV} being the projection

of the magnetic field along the NV axis.

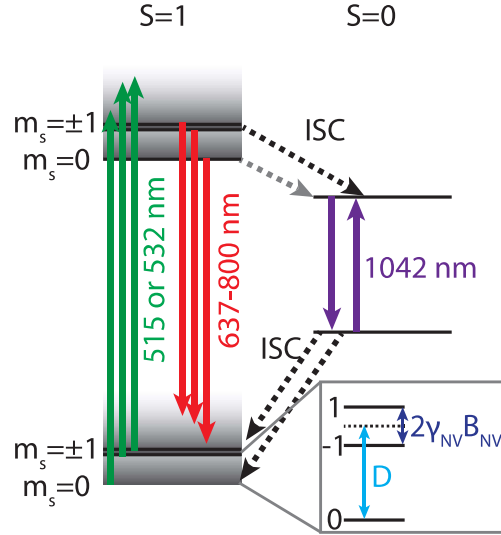


Figure 1.2.4: Energy-level diagram of the NV center. The most important levels for common applications are the $S = 1$ (triplet) ground and excited states and the two singlet ($S = 0$) states. The phonon sidebands for $S = 1$ are indicated by gray color gradients, while being omitted for $S = 0$. The inset shows the substructure of the $S = 1$ ground state with magnetic-field-dependent sublevels that are employed for magnetic-field sensing.

1.2.5 Ground-state Hamiltonian of the NV center

Key for magnetometry with NV centers is, in addition to the optical spin initialization and readout, the existence of magnetically sensitive energy levels. This part of the thesis will therefore provide more details on the theory describing the ground state of the NV center, which contains the sublevels commonly used for magnetometry.

The ground-state Hamiltonian describing the NV center sufficiently for the scope of this work is the following, adapted from [56, 60]:

$$\mathcal{H}/h = \mathcal{H}_{NV} + \mathcal{H}_Z + \mathcal{H}_{\text{hfs}}, \quad (1)$$

where h is the Planck constant, \mathcal{H}_{NV} describes the electronic structure of the NV center without external fields, \mathcal{H}_Z the Zeeman interaction with an external magnetic field and \mathcal{H}_{hfs} the hyperfine interaction with the nitrogen host nucleus.

Furthermore, \mathcal{H}_{NV} can be expanded to

$$\mathcal{H}_{\text{NV}} = (D + \Pi_z)(\hat{S}_z^2 - S(S+1)/3) + \Pi_x(\hat{S}_y^2 - \hat{S}_x^2) - \Pi_y(\hat{S}_x\hat{S}_y + \hat{S}_y\hat{S}_x). \quad (2)$$

Here, $D \approx 2.87$ GHz is the longitudinal zero-field splitting parameter, $\hat{\mathbf{S}}$ is the electron spin with projections $\hat{S}_x, \hat{S}_y, \hat{S}_z$, $\Pi_{x(y,z)}$ are phenomenological, diamond-sample/NV dependent parameters combining local strain and electric fields. In this work and also for the most applications of NV centers, D is the strongest interaction and therefore defines the quantization axis, by convention usually along z .

The Zeeman term represents the central part for magnetometry protocols as it describes the interaction with external magnetic fields:

$$\mathcal{H}_Z = \gamma_{\text{NV}}\mathbf{B} \cdot \hat{\mathbf{S}} + \gamma_{\text{N}}\mathbf{B} \cdot \hat{\mathbf{I}}, \quad (3)$$

where γ_{N} is the nuclear gyromagnetic ratio ($\gamma_{^{15}\text{N}} = -0.43$ kHz/G and $\gamma_{^{14}\text{N}} = 0.3$ kHz/G), $\hat{\mathbf{S}}$ is the nuclear spin, and \mathbf{B} is the external magnetic field.

Additionally, the NV center contains a nuclear spin via the nitrogen nucleus, as both stable nitrogen isotopes have non-zero spin. The nuclear subsystem and its interaction with the electron spin is described by,

$$\mathcal{H}_{\text{hfs}} = A_{\text{hfs}}^{\parallel}\hat{S}_z\hat{I}_z + A_{\text{hfs}}^{\perp}(\hat{S}_x\hat{I}_x + \hat{S}_y\hat{I}_y) + Q(\hat{I}_z^2 - I(I+1)/3). \quad (4)$$

Here, I is the nuclear spin number and $\hat{I}_x, \hat{I}_y, \hat{I}_z$ the components of the corresponding nuclear spin operators. The axial and perpendicular hyperfine parameters are denoted as $A_{\text{hfs}}^{\parallel}$ and A_{hfs}^{\perp} . The nuclear-quadrupole-interaction parameter $Q \approx -5.01$ MHz [61] is only present for $I > 1/2$, i.e. ^{14}N . The two stable nitrogen isotopes are a) ^{14}N with $I = 1$ with a natural abundance of $\approx 99.6\%$ and b) ^{15}N with $I = 1/2$ and a natural abundance of $\approx 0.4\%$. In addition to the presence of the quadrupolar interaction for ^{14}N -containing NV centers, the hyperfine coupling parameters for both stable nuclei also differ. For ^{14}N , $A_{\text{hfs}}^{\parallel} = -2.14$ MHz and $A_{\text{hfs}}^{\perp} = -2.7$ MHz were observed, while the values for ^{15}N are $A_{\text{hfs}}^{\parallel} = +3.03$ MHz and $A_{\text{hfs}}^{\perp} = +3.65$ MHz [61].

On the left side of Fig. 1.2.5, a qualitative depiction of the resulting energy-level scheme, taking into account the most important interactions for magnetometry with NV centers, is shown. The key feature that should be recognized is the magnetic field dependence of the $m_s = \pm 1$ with respect to each other and to the $m_s = 0$ state, which will be used for magnetometry.

The influence of the ^{14}N nuclear spin on the energy-level structure and the respective transitions is shown in the center and right side of Fig. 1.2.5. One can observe that each m_s sublevel is additionally split into three sublevels and that the transition frequencies for different nuclear

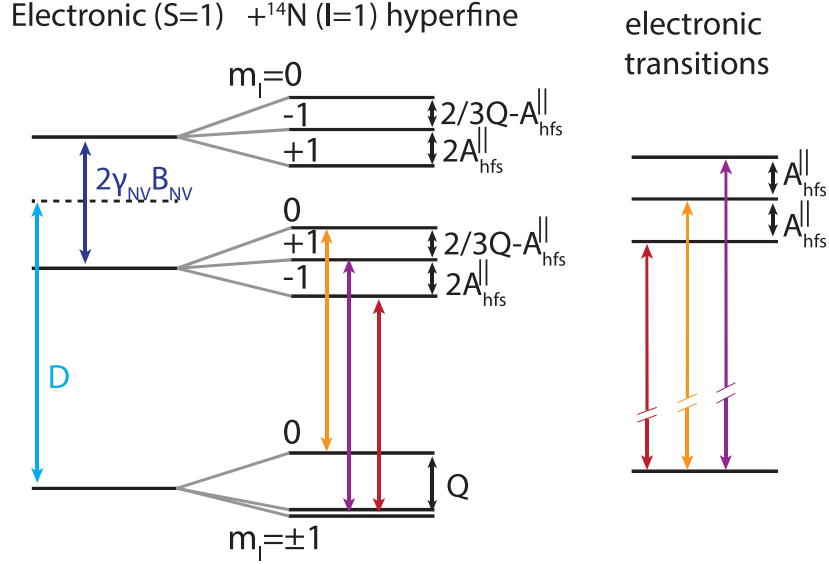


Figure 1.2.5: Left: electronic energy-level structure of an NV center, taking into account the interaction with an external magnetic field via the Zeeman terms. Center: additional splittings of the energy levels occur due to interaction with the ^{14}N (spin-1) host nucleus of the NV center. Right: schematic of the possible (nuclear-spin-conserving) transitions within the NV center's ground state, which differ in their transition frequencies by $A_{\text{hfs}}^{\parallel}$.

spin states are shifted by $\pm A_{\text{hfs}}^{\parallel}$ for $m_s = \pm 1$. In the case of ^{15}N , the levels and the transitions split into doublets [62], which is omitted here since no measurements on NV centers, that contain ^{15}N are presented in this thesis.

1.3 Magnetometry with NV centers

1.3.1 Optically detected magnetic resonance (ODMR)

The most popular and one of the easiest magnetometry protocols with NV centers as sensors is so-called optically detected magnetic resonance spectroscopy. To be more precise, the continuous-wave optically detected magnetic resonance (cw-ODMR) spectroscopy.

In this measurement protocol the NV center(s) is (are) continuously illuminated with green light and the red fluorescence is detected with a photodetector (PD). The green illumination

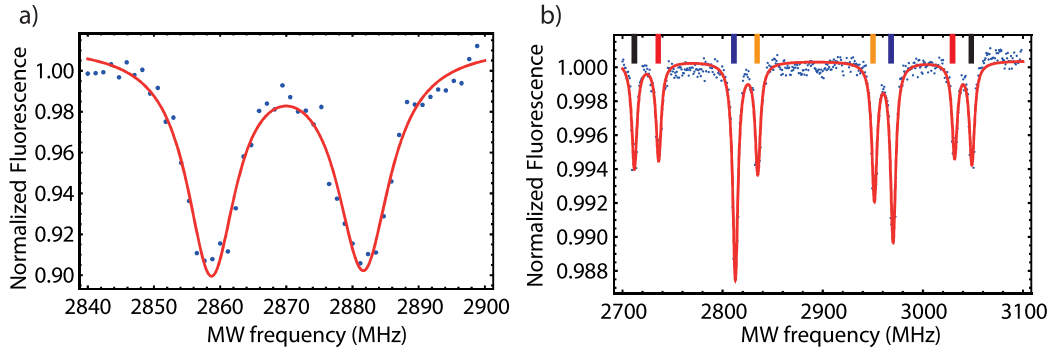


Figure 1.3.6: a) cw-ODMR spectrum of a single NV center. b) cw-ODMR spectrum of an NV ensemble with a bias field applied in an arbitrary direction. Eight peaks are observed because of different magnetic-field projections along the four NV axes for different NV orientations. Dips in the spectrum corresponding to NVs aligned along different axes are indicated with different colors. The hyperfine splitting is not observed in either cw-ODMR spectrum, since the observed linewidth is larger than the hyperfine splitting.

results in a polarization of the NV center into the $m_s = 0$ ground state. Additionally, a cw microwave (MW) field is applied and the frequency of the MW field is scanned. When the applied MW frequency matches the transition frequency between two states $m_s = 0 \rightarrow m_s = \pm 1$, part of the population in the $m_s = 0$ is transferred to (one of) the $m_s = \pm 1$ states. As mentioned earlier, those states have a lower fluorescence rate and therefore the overall fluorescence drops when the MW are on resonance with one of the transitions.

Since the transition frequencies to the $m_s = \pm 1$ states shift in opposite directions and proportional to the magnetic field along the NV axis B_{NV} , the magnetic field is determined by solving

$$B_{\text{NV}} = \frac{\Delta\nu}{2\gamma_{\text{NV}}}, \quad (5)$$

where $\Delta\nu$ is the difference in transition frequencies. Fig. 1.3.6a) shows a cw-ODMR spectrum of a single NV center with a splitting of ≈ 23 MHz corresponding to $B_{\text{NV}} \approx 4.1$ G.

Moreover, as mentioned earlier, there are four equivalent crystallographic axes along which an NV center can be aligned. Even though it is nowadays possible to engineer the NV centers during diamond growth such that they are aligned preferentially along one direction [44, 63], in all diamonds that are used in this work the distribution of NV centers along the possible crystallographic directions is equal. For an arbitrarily oriented magnetic field, this results in four sets of two dips in the ODMR spectrum as the projections of the magnetic field differ

(see Fig.1.3.6b)). The four different sets of dips are marked with colours simplify assignment of the different NV axes. As a direct consequence, this allows for the reconstruction of the full magnetic-field vector, when working with an ensemble of NV centers.

The (photon-shot-noise limited) magnetic sensitivity that can be achieved with the cw-ODMR scheme is given by [31, 64]:

$$\eta_{\text{cw}} \approx \frac{1}{\gamma_{\text{NV}}} \frac{\text{FWHM}_{\text{mr}}}{C\sqrt{\mathcal{R}}} \quad (6)$$

FWHM_{mr} is the full width at half maximum (FWHM) of the observed magnetic resonance (dip) in the spectrum (≈ 9 MHz in Fig.1.3.6a)); C denotes the contrast of the resonance, which is $\approx 10\%$ in Fig.1.3.6a); \mathcal{R} is the photon detection rate, which can differ greatly between experiments especially when comparing single and ensemble NV experiments. For a single NV the detection rate is usually on the order of 100-300 thousand photon counts per second (kcts/s) and can reach up to ≈ 2 Mcts/s for special pillar geometry to enhance photon collection efficiency [65]. For high-density ensembles it is possible to detect fluorescence that is higher than 1 mW, which in turn corresponds to $\approx 3.5 \times 10^{15}$ detected photons per second.

1.3.2 Rabi oscillations

In addition to cw-ODMR measurements, there are a variety of pulsed measurement schemes, where the MWs and the laser illumination are applied in pulses. If a MW field is resonant with one of the NV center's ground-state transitions (determined by ODMR), the NV population starts to oscillate between e.g. the $m_s = 0$ and the $m_s = -1$ state. This effect is called the Rabi cycle. The pulse scheme to detect those Rabi oscillations is shown in Fig.1.3.7a).

A green laser pulse is applied for spin initialization and read-out and is followed by a resonant MW pulse with varying duration τ . As shown in Fig.1.3.7b), the fluorescence oscillates as a function of the length of the pulse length. As explained above, this corresponds to oscillations between m_s sublevels, while the lowest fluorescence rate corresponds to the $m_s \pm 1$ state and the highest to the $m_s = 0$ state. The frequency of the oscillation, the Rabi frequency, is given by

$$\Omega = 2\pi\gamma_{\text{NV}}B_1. \quad (7)$$

γ_{NV} is again the gyromagnetic ratio of the electron and B_1 is the amplitude of the MW field (with frequency ω) which can be described as $B_{\text{MW}} = B_1 \sin(\omega t)$. If the MW frequency is not exactly on resonance, the Rabi frequency increases to,

$$\Omega_{\text{eff}} = \sqrt{\Omega^2 + \Delta^2}. \quad (8)$$

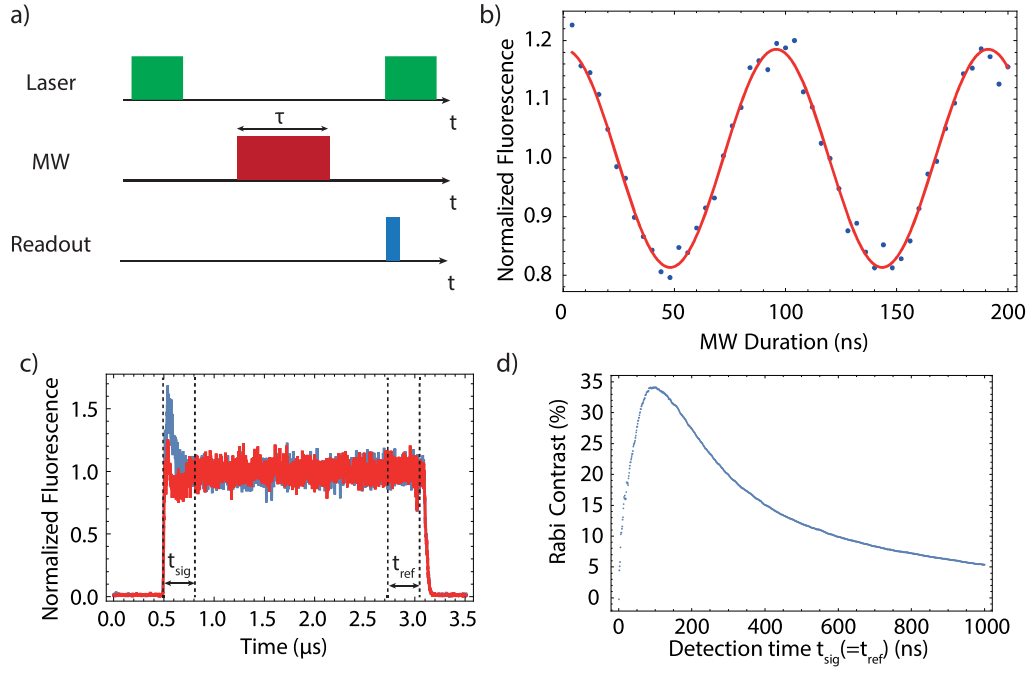


Figure 1.3.7: a) the pulse scheme that is used to acquire Rabi oscillations. First a green laser pulse is used to initialize the NV, then a resonant MW pulse of variable duration is applied and followed by a green read-out laser pulse. b) measured Rabi oscillations of a single NV center. The red curve shows a cosine fit of the data, estimating the Rabi frequency to be 10.49 MHz. c) shows the fluorescence profiles for the $m_s = 0$ (blue) and the $m_s = -1$ state (red), which is used to optimize the readout contrast. t_{sig} and t_{ref} and the dashed lines indicate the signal/detection time and reference time windows during which the photons are considered for signal detection and referencing, respectively. d) demonstrates the optimization process where the relative change in fluorescence between $m_s = 0$ and $m_s = -1$ is calculated for different detection times t_{sig} , starting from the beginning of the laser pulse and normalized by the number of photons collected in the same time span from the end of the laser pulse.

Δ is called the detuning and is given by $\Delta = |\omega - \omega_0|$, with ω_0 being the resonance/transition frequency. Moreover, in the case of $\Delta \neq 0$, the amplitude of the oscillation (A_{eff}) is also decreased compared to an amplitude A_0 for the $\Delta = 0$ case. It is given by:

$$A_{\text{eff}} = \frac{A_0}{1 + \left(\frac{\Delta}{\Omega}\right)^2} \quad (9)$$

As a direct result, with $\Delta \neq 0$, the NV cannot be fully polarized to the $m_s \pm 1$ states. In this work, Rabi oscillations are mostly measured to determine the Rabi frequency, which defines the duration of a π - and $\pi/2$ -pulse. The π -pulse duration is given by $\tau_\pi = 1/2\Omega$. A π -pulse inverts the NV population, i.e. a π -pulse is a 180° rotation on the so-called Bloch sphere (details can be found elsewhere [66, 67]).

Correspondingly, a $\pi/2$ -pulse is a 90° rotation and usually used to create a superposition state or rotate the NV back to one of the eigenstates states for readout.

To achieve optimal readout fidelity and, with that, sensitivity, it is important to analyze the repolarization process/ timescales within the green laser pulse. Fig. 1.3.7c) shows the fluorescence profile within a 2.5 μs laser pulse for an NV initially being in the $m_s = 0$ state (blue) and in the $m_s = -1$ state (red). One observes that at the beginning of the pulse the fluorescence rates differ significantly, while they are equal after more than ≈ 500 ns measured from the beginning of the pulse. This is a result of the fact that the same mechanism that leads to reduced fluorescence when the NV is in $m_s = \pm 1$ also leads to reinitialization to $m_s = 0$ and therefore it is important to choose the time windows for spin readout accordingly. On the other hand, the reinitialized steady-state fluorescence at the end of each laser pulse can be used to normalize the signal and therefore eliminate slower laser-intensity variations.

Fig. 1.3.7d) shows the optimization process for maximum contrast in the spin readout. The contrast, i.e. the number of collected photons within t_{sig} from the beginning of the pulse is divided by the reference time window t_{ref} . For simplicity both time windows are set to the same length. When $t_{\text{sig}} \approx 100$ ns after the start of the laser pulse, a maximum of $\approx 35\%$ contrast is reached and decreases again for larger t_{sig} , as the NV center starts to polarize back into $m_s = 0$. This optimization allows for maximum contrast in all further pulsed experiments and is therefore vital to achieve maximum sensitivity in pulsed measurement protocols.

1.3.3 Pulsed ODMR

A progression of cw-ODMR is the pulsed ODMR scheme, which, as the name suggests, uses pulsed MW and laser fields instead of cw fields. As known from atomic spectroscopy, high probe-light power can result in power broadening of the observed spectrum [68, 69]. The same

is true for the NV center, hence a pulsed measurement scheme can decrease the linewidth without reducing the contrast, and with that enhance magnetic sensitivity [70].

The measurement sequence consists of a $\approx 3 \mu\text{s}$ laser pulse, followed by a MW π -pulse with a duration of $\tau_\pi = 0.5/\Omega$ (see Fig. 1.3.8a)). This sequence is then repeated, while the MW frequency is changed and an ODMR spectrum is detected.

In Fig. 1.3.8b) an ODMR spectrum obtained by pulsed ODMR is shown. The overall spectrum is observed using strong MW pulses with π -pulse duration of $\approx 50 \text{ ns}$, leading to a full width at half maximum (FWHM) of $\approx 10 \text{ MHz}$. To observe the hyperfine splitting originating from the ^{14}N nucleus, the MW pulse length was increased to about $3 \mu\text{s}$ and the power adjusted accordingly. This is necessary to keep performing an exact π -pulse on the NV. As a result, the observed linewidth decreases to $\text{FWHM} \approx 350 \text{ kHz}$ and the hyperfine splitting of $\approx 2.14 \text{ MHz}$ can be observed.

Furthermore, the contrast is reduced to $\approx 8 \%$ in this case. This results from the fact that during pulsed ODMR with a strong π -pulse, all three hyperfine components are observed simultaneously and therefore their contrasts adds up. In the case of a weak and long MW pulse as in the inset, each hyperfine component is observed individually and therefore one can only obtain $\approx 10 \%$ contrast. In principle, both, full contrast of all three hyperfine components and narrow linewidths can be achieved by applying a frequency “trident” with a separation between the prongs of 2.14 MHz (during the MW pulse) [21, 31].

Furthermore, as shown in Ref. [70] the optimum sensitivity is achieved when $\tau_\pi \approx T_2^*$. T_2^* is called the dephasing time and will be explained in a bit more detail in the next section. Simply speaking, in that case the MW power broadening during the π -pulse is equal to the minimal observable linewidth of the transition $\text{FWHM} \approx 1/(\pi T_2^*)$, usually dominated by the magnetic noise generated by other magnetic impurities in the vicinity of the NV center, e.g. nuclear spins or paramagnetic centers [31]. For $\tau_\pi < T_2^*$ and decreasing τ the linewidth remains constant, as it is not dominated by power broadening anymore, and the contrast starts decreasing as well, resulting in a reduced sensitivity.

With an optimized pulsed ODMR scheme the achievable shot-noise-limited sensitivity is given by [31, 64]:

$$\eta_{\text{pulsed}} \approx \frac{1}{\pi\gamma_{\text{NV}}} \frac{1}{C\sqrt{\mathcal{R}t_{\text{R}}/t_{\text{seq}}T_2^*}} \quad (10)$$

Here, \mathcal{R} is the detected fluorescence rate during the laser pulse, t_{R} is the time of the spin readout during the laser pulse and t_{seq} is the duration of the measurement sequence, i.e. the time between two laser pulses.

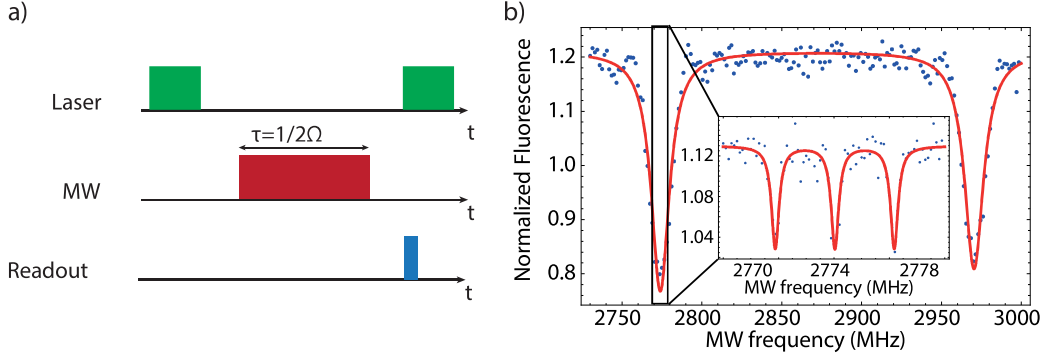


Figure 1.3.8: a) the pulse scheme that is used for pulsed ODMR. First a green laser pulse is used to initialize the NV, then a MW pulse of fixed length is applied and followed by a green read-out laser pulse. This is repeated for different MW frequencies to obtain an ODMR spectrum of a single NV center. b) measured pulsed ODMR spectrum. A contrast of $\approx 30\%$ is observed. The inset shows a low-power pulsed ODMR spectrum (long and weak MW pulse), where the three different hyperfine components resulting from the interaction with the host ^{14}N nuclear spin with a typical separation of 2.14 MHz are resolved.

1.3.4 Ramsey interferometry

Another pulse sequence that is used in this work, is the so-called Ramsey sequence. This sequence was originally designed by Ramsey to circumvent the technical difficulty of applying a small homogeneous field in a molecular beam experiment [71]. He showed, that by applying two short and strong $\pi/2$ -pulses with time spacing τ one can achieve a similar (slightly improved) linewidth as compared to a fully optimized pulsed ODMR scheme as explained before [71].

In the original work by Ramsey, the frequency of the applied field was changed, while nowadays it is more common to vary the free evolution time to observe a signal.

The pulse scheme is shown in Fig. 1.3.9 a). First the initializing laser pulse is applied, followed by a $\pi/2$ -pulse which creates a superposition state of $m_s = 0$ and $m_s = \pm 1$. In general, a superposition state of a two-level system can be described by

$$|\Phi\rangle = \cos\frac{\theta}{2} |m_s = 0\rangle + e^{i\varphi} \sin\frac{\theta}{2} |m_s = -1\rangle. \quad (11)$$

By convention $\varphi = 0$ corresponds to the alignment along $+x$ -axis on the Bloch sphere. After the first $\pi/2$ pulse, the NV is described by the following superposition state: $\frac{1}{\sqrt{2}} |(m_s = 0)\rangle + e^{i\varphi_0} \frac{1}{\sqrt{2}} |-1\rangle$. Often φ_0 is defined to be along the x or y axis of the Bloch sphere, i.e. $\varphi_0 = 0$

or $\varphi_0 = \pi/2$. After the initialization, a waiting time τ , also called free evolution time, follows. During this time an additional phase φ_{ram} is accumulated and is given by [31, 72]:

$$\varphi_{\text{ram}} = 2\pi \gamma_{\text{NV}} \int_0^\tau B_{\text{NV}}(t) dt \quad (12)$$

The sequence is terminated with another $\pi/2$ pulse which rotates the NV back to either the $|0\rangle$ or $|-1\rangle$ state or a superposition, depending on the accumulated phase. This rotation to $m_s = 0$ can be realized by either applying a $3\pi/2$ -pulse instead of the last $\pi/2$ -pulse or by applying a $-\pi/2$ -pulse. A $-\pi/2$ -pulse can be achieved by changing the phase of the MW pulse by 180° and can be very useful for sanity checks or to study the fidelity of a (more complicated) pulse sequence.

An example of such a measurement is shown in Fig. 1.3.9 b). The blue curve shows data that is obtained with a regular $\pi/2$ -pulse as final MW pulse while the red curve shows data obtained with a $\pi/2$ -pulse as final pulse. One can observe that, as expected, the two graphs are complementary to each other.

Fig. 1.3.9 c) then shows the calculated difference between the two data sets, which oscillates around zero. The timescale at which the oscillation amplitude decays is the aforementioned dephasing time $T_2^* \approx 0.8 \mu\text{s}$.

Last but not least, Fig. 1.3.9 d) shows the fast Fourier transform (FFT) of c) and in the spectrum, three different frequencies can be clearly observed. These frequencies are the three hyperfine components separated by 2.14 MHz, which all have a different detuning Δ to the applied MW frequency and therefore oscillate at different frequencies in the Ramsey experiment.

To summarize, the photon-shot-noise-limited sensitivity that can be achieved with a Ramsey measurement is also [31, 64]:

$$\eta_{\text{Ramsey}} \approx \frac{1}{\pi \gamma_{\text{NV}}} \frac{1}{C \sqrt{\mathcal{R} t_{\text{R}} / t_{\text{seq}} T_2^*}} \quad (13)$$

In general, it depends on the specific experiment which measurement scheme is favourable, as they all differ in complexity, requirements on equipment and finally, sensitivity.

With this, the introduction to NV centers, and in particular magnetometry with NV centers, is sufficiently completed to understand all basic principles for NV-center magnetometry that are necessary to follow and comprehend the works presented below. It should be noted, that all the above-mentioned protocols are all dc protocols, i.e. they are used to measure constant (dc) magnetic fields. In addition, a variety of ac sensing protocols exists, which are omitted here as they are not used in the remainder of this thesis, but usually lead to higher sensitivities in narrow frequency bands [11, 29, 72–74].

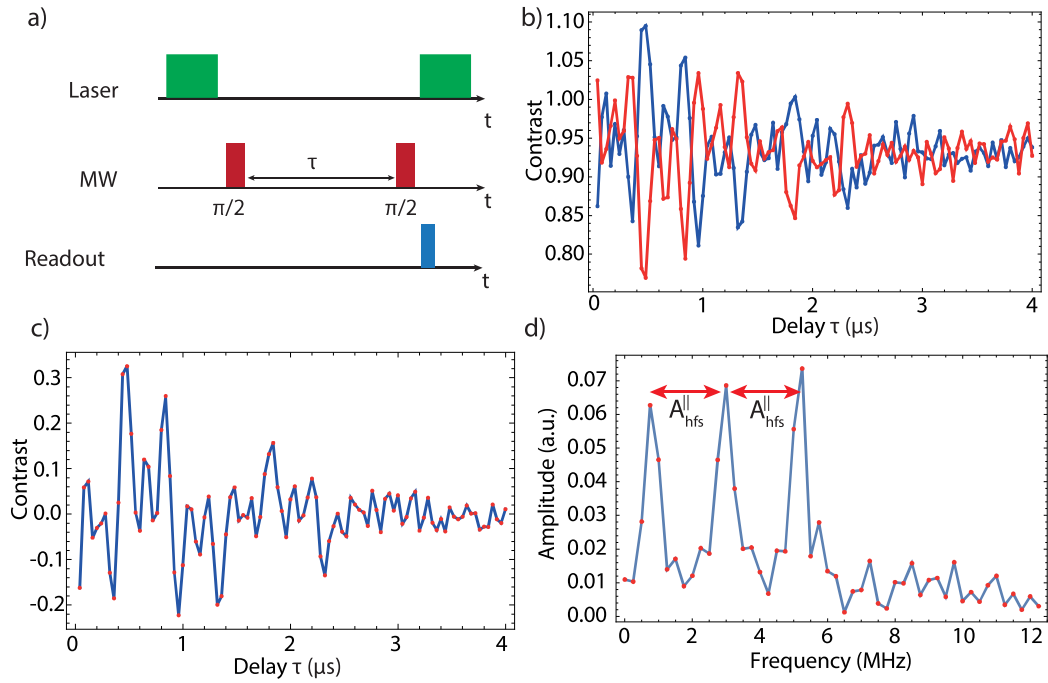


Figure 1.3.9: a) the pulse scheme that is used to perform Ramsey interferometry. First a green laser pulse is used to initialize the NV, then a resonant $\pi/2$ -MW pulse is applied, followed by a variable free precession time τ , a second $\pi/2$ -pulse and a green read-out laser pulse. b) measured Ramsey fringes of a single NV center. The blue graph shows the data acquired with a normal final $\pi/2$ -pulse, while the red graph is obtained by using a $-\pi/2$ pulse at the end. c) shows the difference between the blue and red data in b). d) the Fourier transform of the data in c) showing three distinct frequencies corresponding to the three hyperfine components in the ODMR spectrum.

To summarize shortly, the diamond structure and synthesis methods were presented. Crystallographic defects were introduced with a focus on NV centers and their creation. Afterwards, the NV-center's energy-level structure was explained and the ground state Hamiltonian was discussed in some detail. In the end, different magnetometry protocols and their respective sensitivities were described.

2.2 Introduction

Studying the physics of vortices in type-II superconductors (SCs) is a key challenge in the field of condensed-matter physics, which in the past, has been addressed by various methods. For example, a scanning superconducting quantum-interference device (SQUID) [75–78], scanning Hall-probe magnetometry [79–81], Bitter decoration [82–84], transmission-electron microscopy (TEM)[85, 86], scanning tunneling microscopy and spectroscopy[87], Lorentz microscopy[88], and magneto-optical imaging [89, 90] have been used to image vortices in type-II superconductors. Recently, a method has been proposed[91] and realized[18], which uses a single nitrogen-vacancy (NV) center in a scanning diamond tip to study such vortices. Using NV centers enables quantitative noninvasive studies of the vortices over a wide temperature range, which is not achievable with the previously mentioned methods. In this work, ensembles of NV centers in diamond are used for an alternative approach of imaging vortices. Utilizing ensembles has the important advantage of not requiring a physical scan of the sample (or the sensor), thereby opening the door for fast imaging up to video frame rates[92]. Here, we use this technique in a wide-field microscope to image vortices in an yttrium-barium-copper-oxide (YBCO) thin film.

NV centers in diamond are point defects in the diamond lattice and have a magnetic-field-dependent energy-level splitting, which can be driven by resonant microwaves and read out optically by excitation with green light and collection of red NV fluorescence[64]. Magnetometry with NV centers is a widely used technique because of its combination of sensitivity and high spatial resolution. It is applicable in a wide temperature range from cryogenic to ambient temperatures[18, 93, 94]; in addition, the method enables the determination of both the absolute value and the direction of the magnetic field[13, 64, 95].

2.3 Experimental setup

The experimental setup located at Ben-Gurion University of the Negev incorporates a wide-field-imaging microscope (see Fig.2.4.1a) with the imaging target placed in a continuous-flow helium cryostat. The superconducting sample, a thin YBCO film (thickness ≈ 250 nm), is placed onto the cold finger inside the cryostat and a diamond microslab (thickness ≈ 2 μ m) with {100} surfaces is placed flat on top of the superconductor. The proper engineering of the SC-diamond interface and, in particular, the resulting NV-SC distance is a crucial enabling factor for this work. Commonly used diamond plates of dimensions on the order of $3 \times 3 \times 0.5$ mm³ do not allow us to detect individual vortices. Because of the distance between the diamond plate and the SC, it was only possible to measure the averaged homogeneous field

penetrating the SC[7]. In addition, the properties of the NV centers in the used diamond plates are not able to detect a magnetic field below 0.1 mT (see Sec.2.4 and Fig.2.4.1c). This means that, in order to observe individual vortices, the distance between the SC and the diamond has to be below approximately 1 μm . To achieve this, thin diamond plates with dimensions of $20 \times 10 \times 2 \mu\text{m}^3$, with a near-surface NV-center rich layer of approximately 70-nm thickness, are fabricated and placed onto the SC (see methods). Microwave fields are applied by a wire (see Fig.2.4.1a, inset), which is mounted on the homebuilt cryostat window to keep the heat transfer to the SC as low as possible, while still keeping the wire close to the diamond. The fluorescence is detected using a CCD camera with a pixel size of $16 \times 16 \mu\text{m}^2$.

2.4 Results

2.4.1 Optically detected magnetic-resonance images

To generate vortices, the sample is field-cooled in a magnetic field of approximately 0.18 mT, applied perpendicular to the surface of the YBCO film. Optically detected magnetic-resonance (ODMR) spectra are taken for every pixel of the camera, each of which corresponds to an area of $0.16 \times 0.16 \mu\text{m}^2$ on the sample. The ODMR spectra are obtained by comparing NV fluorescence rates with and without applied microwaves while scanning the MW frequency from 2.84 GHz to 2.91 GHz. The fluorescence contrast is calculated as $C = (N_{\text{on}} - N_{\text{off}})/(N_{\text{on}} + N_{\text{off}})$, where $N_{\text{on(off)}}$ is the photon detection rate, while the applied microwave field is on (off). The NV-center ground state is a spin-1 system, leading to three states with $m_s = -1, 0$, and $+1$. In the absence of symmetry-breaking fields, the $m_s = \pm 1$ states are degenerate, leading to the same transition frequency from the $m_s = 0$ state to the $m_s = \pm 1$ states of 2.87 GHz at room temperature (2.88 GHz at cryogenic temperatures). The transition frequencies get split by a magnetic field along the NV axis where the splitting is given by $\Delta\nu_{\pm 1} = 2\gamma_{NV}B_{NV}$, with $\gamma_{NV} = 28 \text{ MHz/mT}$ and B_{NV} the magnetic field along the NV axis. For our diamond samples and at temperatures slightly above the SC phase transition, even at zero field, a splitting (approximately 6 MHz) in the ODMR spectra occurs due to strain in the diamond lattice[64]. This strain mixes the $m_s = \pm 1$ states, so that m_s are no longer good quantum numbers, and results in a nonlinear relation of $\Delta\nu_{\pm 1}(B_{NV}) = 2\sqrt{(\gamma_{NV}B_{NV})^2 + E^2}$, with E being the strain splitting for low magnetic fields[96]. For ensembles of NV centers, there are in general four different NV axes with corresponding different field projections that need to be considered. For the $\{100\}$ diamonds used in this work, the field projection for a field perpendicular to the surface is the same for all NV orientations.

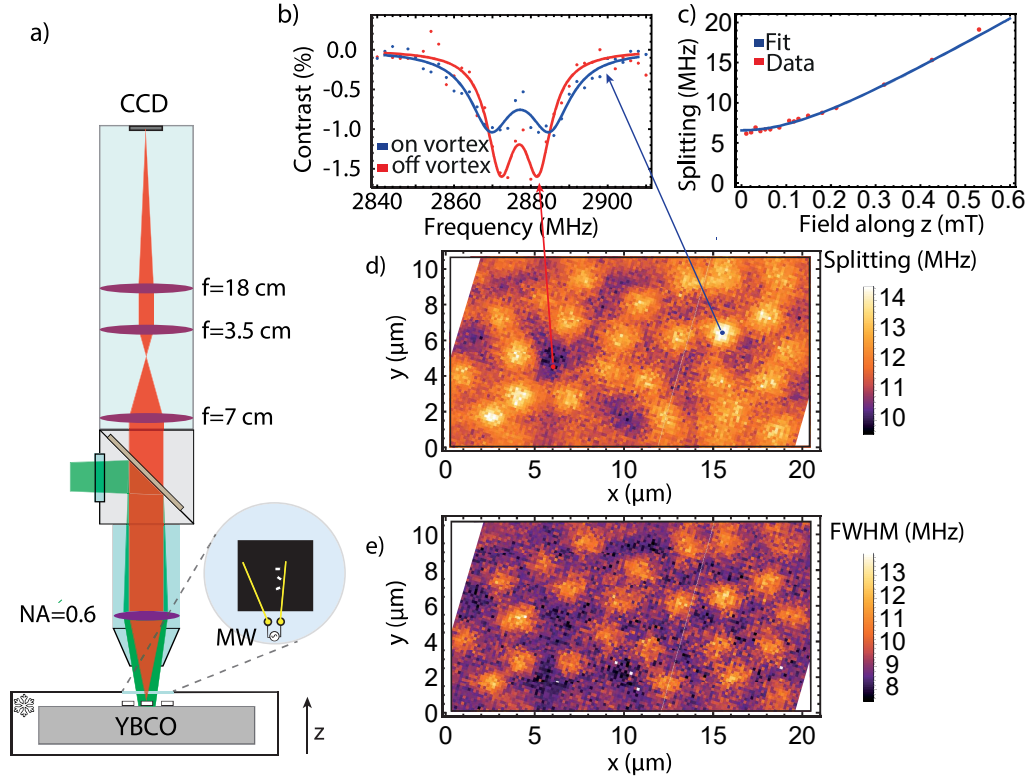


Figure 2.4.1: (a) Schematic of the experimental setup. (b) ODMR spectrum for a pixel on top of the vortex and for a pixel outside of the vortex stray field, which is approximately 0.38 mT in the center of the vortex. (c) Calibration of the magnetic field in the nonlinear regime at low fields. (d) Map of the splitting between the two ODMR peaks and e) map of the width of the ODMR peaks. Vortices are identified by an increase in the splitting between the ODMR peaks, which is attributed to the magnetic stray field of the vortices. In addition, the vortices' stray field leads to a broadening of the peaks, which is generated by field inhomogeneities over the detection volume. The acquisition time for the images (d),(e) is approximately 11 min.

To determine the ODMR splitting, the recorded data are fitted to two Lorentzians (Fig.2.4.1b) for each pixel, and color maps of the peak width and splitting are created (Fig. 2.4.1d, e). The splitting of the two peaks differs by approximately 4 MHz depending on the point of observation with respect to the vortex center. Additionally, the width of the peaks also changes by an amount of 4 MHz, which is attributed to magnetic-field gradients averaged over the optical resolution of approximately 500 nm and to vibrations that are of similar mag-

nitude as the optical resolution. To illustrate these effects more explicitly, Fig.2.4.1b shows two ODMR spectra, one recorded on a vortex and one far from a vortex. Even though the change in splitting is on the same order as the splitting due to strain at zero field (see below), it is possible to determine the magnetic field above the vortices. To do this, we calibrate the splitting between the two peaks as a function of magnetic field by applying a known, out-of-plane magnetic field to the diamond and the data are fitted (see Fig.2.4.1c) using the relation mentioned above. The angle between the NV centers and the applied field is considered by using $B_{NV} = B_z/\sqrt{3}$ and the strain splitting E is determined to be 3.29 (5) MHz.

Using this calibration, we determine the maximum field perpendicular to the SC above the vortices to be between approximately 0.36 mT and 0.4 mT. Following the model used in Ref.[97] and considering a bulk London penetration depth $\lambda_L = 250$ nm[18], we see that these fields correspond to an average distance between the YBCO and the NV layer of approximately 550 nm. This distance is larger than expected from the roughnesses of the SC (≈ 100 nm) and the diamond plate (approximately 3 nm) and the depth of the diamond layer ($d_{NV} \approx 15 - 85$ nm) and it probably originates from dust particles on the surface of the SC and outliers in the roughness of the SC. Decreasing the distance between the SC and the diamond in the future would shrink the observed size of the vortices and allow us to extract more precise information on the magnetic field.

2.4.2 Single-frequency images

To reduce the image acquisition time, instead of taking whole ODMR spectra for every pixel, images of vortices are obtained by determining the contrast for every pixel for only a single MW frequency (e.g., 2.876 GHz) applied to drive the NV spins. The magnetic field of the vortex leads to a splitting of this resonance and, therefore, to an increased fluorescence at the position of the vortices in the presence of the MW-driving field (see Fig.2.4.2). These images are taken for different cooling fields, ranging from $B_{cool} \approx 0$ to 0.18 mT, applied along the direction normal to the SC film. As expected, the different cooling fields led to different vortex densities in the SC. The expected number of vortices is $N = B_{cool} A/\Phi_0$, where $\Phi_0 = h/(2e) = 2.07$ mT $\cdot\mu\text{m}^2$ is the magnetic flux quantum, B_{cool} is the magnetic cooling field, and A is the investigated area. For the dimensions of our sensitive area, which is the area of the diamond microslab of $200 \mu\text{m}^2$, this leads to $N/B_{cool} \approx 100$ mT $^{-1}$. Figure 2.4.2(d) compares the measured number of vortices with the theoretical expectation and shows good agreement between the two.

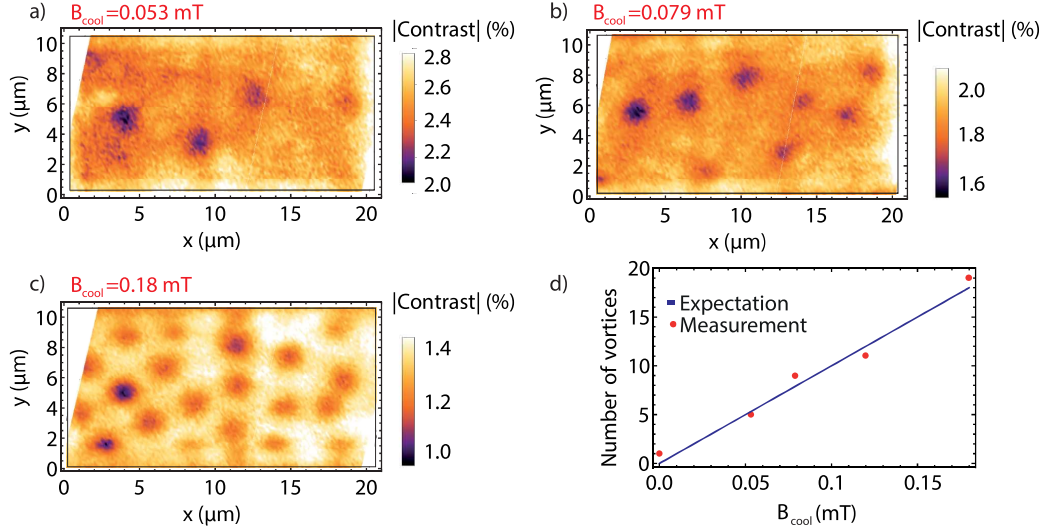


Figure 2.4.2: (a)-(c) Single-frequency images (acquisition time of approximately 80 s) of vortices obtained using microwaves resonant with the NV-spin transition at zero magnetic field (2.876 GHz). Images are taken for a magnetic field (B_{cool}) present during the cooling through the metal-superconductor phase transition with $B_{\text{cool}} = 0.053, 0.079,$ and 0.18 mT . An increase in the number of vortices can be observed when the field is increased. (d) The observed number of vortices as well as the expected number of vortices in the given field of view of $200 \mu\text{m}^2$ for different fields.

2.4.3 Pinning

Another important phenomenon in type-II SC is pinning[98], where the magnetic flux (i.e. vortices) is trapped within the SC due to disorder, even when the external field is turned off. This effect is associated with defects in the superconductor that pin the vortices into their positions. To study pinning, a single-frequency image of the vortex distribution, with and without the applied magnetic field after the cooldown, are taken (Fig.2.4.3). The same vortices can be identified in both images, which means that the pinning is strong enough to trap all the vortices that were previously created, extending the results of an earlier study using ensembles of NV centers[7], where individual vortices could not be resolved.

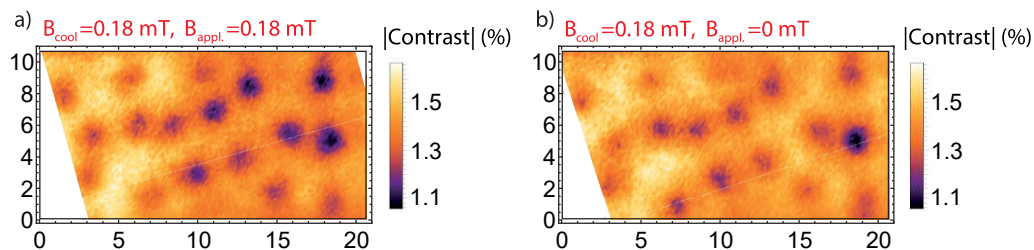


Figure 2.4.3: (a) A single-frequency map (acquisition time of approximately 80 s) with the applied magnetic field. (b) A map after the magnetic field is turned off after reaching the SC phase. Both pictures show the same vortex pattern due to strong pinning in the SC sample.

2.5 Conclusion

A novel technique is presented enabling wide-field imaging of vortices in SCs using NV centers in diamond. By using microfabricated diamond plates, it is possible to reduce the sample-NV distance, which allows us to study the stray magnetic field of vortices in a type-II SC. ODMR spectra are obtained to determine the magnetic-field magnitude from which the distance between the SC and the diamond is calculated to be less than $1 \mu\text{m}$. It is possible to reduce the acquisition time for an entire image using a single frequency. Single-frequency images are taken for different cooling fields and the obtained number of vortices is compared to the theoretical expectations. In addition, pinning of the vortices in the SC is observed. To improve this technique, one could, for example, use a diamond with less strain to enhance the sensitivity at low magnetic fields or use a $\{111\}$ diamond with preferential NV-center orientation[63], leading to an increase in contrast. In addition, the use of a diamond with $\{111\}$ surfaces would align the NV axis of one of the orientations with the magnetic field of the vortices and, therefore, increase the resulting splitting in the ODMR spectrum. Future experiments will focus on more detailed studies of the vortices and their dynamics, such as vortex oscillations in their pinning potential. Using the presented method, such oscillations can be sensed from dc up to several MHz[94, 99]. The implementation of pulsed measurement schemes would in addition enhance the sensitivity to ac fields[64, 100]. Moreover, this technique can be applied as a universal tool to precisely measure the magnetic structures of thin films and/or surfaces.

2.6 Appendix

2.6.1 Methods

2.6.1.1 Sample preparation

The diamond plates are fabricated using electron-beam lithography and plasma etching[101] of an “optical grade” Element 6 diamond (produced via chemical vapor deposition (CVD)) with {100} surfaces and an initial nitrogen concentration below 1 ppm. The NV-rich layer close to the surface of the diamond is created using ion implantation of nitrogen ions with energies of 10, 35, and 50 keV. The diamond is subsequently annealed at 800°C for 10 h and at 1200°C for 2 h to form the NV centers. Assuming a conversion efficiency of approximately 5%[52], this process results in an NV-center density of approximately 3.7 ppm within the implanted layer. This result corresponds to a mean separation of approximately 11.4 nm between the NV centers. The plates are broken out of an array[102] using a micromanipulator and then placed on the SC. In this procedure, we cannot control whether the implanted side is facing toward the diamond. To increase the probability of finding a diamond positioned with the correct orientation, several plates are placed on top of the SC. For a superconductor, a commercially available YBCO thin film from Ceraco consisting of 250 nm of YBCO grown on a sapphire wafer with a 40-nm buffer of CeO₂ was used. This growth process leads to an orientation of the YBCO c axis perpendicular to the surface of the thin film. The critical temperature of the SC sample is approximately 87 K (according to the company specifications). In addition, we are able to transfer the diamond plates to other samples using a sharp needle. This is due to the fact that electrostatic forces between the needle and the diamond are stronger than the van der Waals forces between the SC and the diamond. The low van der Waals interaction is consistent with the surface roughness and the unexpectedly large distance between the SC and diamond plate.

2.6.1.2 Experimental setup

The experimental setup consists of a continuous-flow helium cryostat (Janis model ST-500) and a homebuilt wide-field fluorescence microscope. The green excitation light is generated by a Gem 532 laser (Laser Quantum) reflected with a dichroic mirror (Semrock FF635-Di01-25x36) and focused onto the sample with an Olympus LUCPLFLN40XRC objective with a $\times 40$ magnification and a NA = 0.6. The fluorescence is collected through the same path; after it traverses the dichroic mirror and a telescope (to increase the magnification by a factor of 2) it is focused on the camera [Andor iXon 897 electron-multiplying charge-coupled device

(EMCCD) camera, with pixel size $16 \times 16 \mu\text{m}^2$] with a 180-mm tube lens.

2.6.2 Acknowledgments

We thank [REDACTED] for fruitful discussions. This work was supported in part by the DFG DIP project Ref. FO 703/2-1, by Swiss NFS grants No. 142497 and 155845 and by the Swiss Nanoscience Institute. This work is also partially supported by the Israeli Science Foundation.

3 Imaging Topological Spin Structures Using Light-Polarization and Magnetic Microscopy

The following chapter has been, apart from minor formatting and style changes, published as shown below in a peer-review journal. The reference to the published manuscript is:

T. Lenz, [REDACTED]

[REDACTED]. Imaging topological Spin Structures Using Light-Polarization and Magnetic Microscopy. *Phys. Rev. Appl.*, 15(02404), 2021.

I co-authored this work, contributing in setup design and construction, data-acquisition, data analysis, interpretation of the results, and in preparing the manuscript for publication.

3.1 Abstract

We present an imaging modality that enables detection of magnetic moments and their resulting stray magnetic fields. We use wide-field magnetic imaging that employs a diamond-based magnetometer and has combined magneto-optic detection (e.g. magneto-optic Kerr effect) capabilities. We employ such an instrument to image magnetic (stripe) domains in multilayered ferromagnetic structures.

3.2 Introduction

Understanding the behaviour of spins and charges in magnetic systems is at the heart of condensed matter physics, and intense ongoing research activities are focused on developing and understanding these. This understanding is key towards the generation of faster, smaller, and more energy-efficient magnetic technologies [103, 104].

The success of all research activities relies on advances in theory and materials synthesis, but most critically on sensitive probes. These allow for the determination of their static and dynamic spin configurations and current distributions, which enable an improved understanding of the interplay between the spin-spin and spin-orbit interactions in these systems. To achieve this, several powerful techniques for real-space probing of magnetic structures are employed, such as spin-polarized low-energy electron microscopy [105, 106] and X-ray magnetic circular dichroism [107, 108] both of which are sensitive to the magnetization distribution of the structures.

An alternative approach is the detection of the stray magnetic fields generated by the magnetic textures. Techniques such as magnetic resonance force microscopy [109, 110] and scanning magnetometry using superconducting quantum interference devices (SQUIDs) [111, 112], allow for real-space imaging of the stray magnetic fields emanating from magnetic structures. However, these techniques typically operate over a narrow range of environmental conditions, and in some cases can have magnetic (perturbative) back-action on the devices under investigation.

Magnetometry based on the electron spin of nitrogen-vacancy (NV) defects in diamond has emerged as versatile, highly sensitive stray-field probe for the non-invasive study of magnetic systems [113]. Diamond-based magnetometers can operate from cryogenic to above room temperature environments, have a dynamic range spanning at least nine decades (DC-GHz), and allow for sensor/sample distances as small as a few nanometers. With this, they provide access to static and dynamic magnetic/electric phenomena with diffraction-limited to nanoscale spatial resolution depending on the imaging modality. Most crucially, NV-based magnetometry is magnetically non-perturbative and works under a wide range of external magnetic and electrical fields.

Scanning NV-based magnetic microscopy utilizes a diamond nanocrystal that hosts a single NV center attached to the tip of an atomic force microscope and has already been successfully applied in studies of emerging magnetic phe-

nomena. Prominent examples are the case of nanoscale imaging and control of domain-wall hopping in ultrathin ferromagnets [19] and magnetic wires [114], imaging of non-collinear antiferromagnetic order in magnetic thin films [20], the direct measurement of interfacial Dzyaloshinskii-Moriya interaction in ferromagnetic multilayer heterostructures [115], and even in identifying the morphology of isolated skyrmions in ultrathin magnetic films [116, 117]. Scanning NV-based magnetometry is highly sensitive and produces magnetic field maps of a sample with spatial resolution ultimately limited by the atomic size of the tip. However, similarly to magnetic force microscopy, its operation requires specific environmental conditions and is not suitable for wide-field inspection of dynamics at fast time scales (\sim ms). An alternative is wide-field NV-based magnetic microscopy that employs ensembles of NV centers within a diamond crystal, and allows for magnetic imaging with an unprecedented combination of temporal (ms) and spatial (diffraction-limited) resolution. State-of-the-art experimental demonstrations have demonstrated sub- μ T $\mu\text{m}/\sqrt{\text{Hz}}$ magnetometric sensitivities over wide fields-of-view (FOV) (as large as $\sim 1 \text{ mm}^2$) [16, 118–120].

An additional merit in using NV-based magnetometry is the possibility to simultaneously measure all Cartesian components of static/dynamic magnetic fields [16, 41]. This becomes vital when one wishes to identify, for instance, the type and the chirality of domain walls of skyrmions in magnetic multilayer stacks [19, 121]. However, even with the employment of vector magnetometric protocols, reconstruction of the magnetic spin-structure topology based on the detected stray magnetic fields is an under-constrained inverse problem [113, 121, 122]. In other words, this means an infinite number of magnetic topologies can give rise to similar stray magnetic-field patterns. Therefore, a straightforward solution is the implementation of a detection modality that enables the detection of both the magnetization and its resulting stray magnetic fields.

We present here an imaging modality that allows for the detection of both magnetic moments and their resulting stray magnetic fields. Such an imaging system

consists of a polarization-sensitive epifluorescent microscope that incorporates a diamond sensor and exploits the radiation required for the magnetometric measurements to perform magneto-optic Kerr effect (MOKE) measurements [123]. Such an instrument allows for combined detection of magnetization and their resultant stray magnetic fields, while being magnetically non-perturbative and operable over a broad temperature range, making it an ideal tool for the study of magnetic structures and their dynamics under a wide range of environmental conditions. We wish to emphasize here that a MOKE measurement is an indirect way of detecting the magnetic moments via changes in the polarization of light upon reflection of a magnetic surface. However, this polarization signal can be translated to magnetization using the material’s specific Kerr constant, which we can obtain, for instance, using a SQUID-based calibration measurement.

3.3 Principles of magneto-optical and wide-field magnetic imaging

3.3.1 NV-based magnetic imaging

The NV center in diamond consists of a substitutional nitrogen atom in the carbon lattice adjacent to a vacancy. The negatively charged NV center (NV^-) has an electronic spin-triplet ground state (${}^3\text{A}_2$; $S = 1$) with magnetic Zeeman sublevels $m_s = \{-1, 0, +1\}$ (quantized along the N-V binding axis). Moreover, it has an axial zero-field splitting of ≈ 2.87 GHz between the $m_s = 0$ and $m_s = \pm 1$ sublevels, whose energies shift in response to local magnetic fields, crystal stress, temperature changes, and electric fields (Fig. 3.3.1 (a)). The spin state of the NV center can be initialized (polarized to the $m_s = 0$ sublevel) using (continuous or pulsed) optical excitation (typically with $\lambda = 532$ nm) and readout through spin-dependent photoluminescence (PL): the $m_s = 0$ sublevel exhibits a higher fluorescence rate under illumination than the $m_s = \pm 1$ sublevels. Applying a small external magnetic field along the NV quantization axis lifts the degeneracy of the $m_s = \pm 1$ magnetic sub-levels, and magnetic-field measurements are consequently possible via the precise measurement of the NV spin-resonance frequencies. This is typically done by sweeping the frequency of an externally

applied microwave (MW) driving field while monitoring the spin-dependent photoluminescence, thus allowing for NV-fluorescence-based magnetometry by optically detected magnetic resonance (ODMR) spectroscopy. Alternative magnetometric modalities that rely on absorption- or photocurrent-based detection schemes [13, 124] exist as well, but are not employed in this work. In high quality diamond sensors, the attainable ODMR linewidth is narrow enough to observe the NV-center’s hyperfine structure, i.e. the coupling between the host nitrogen nucleus (99.6% of ^{14}N in natural abundance, for which $I_N = 1$) and the unpaired NV electron spin. For the case of ^{14}N , every observed ODMR peak splits into a triplet with a separation of $A_{hfs} \approx 2.16$ MHz [61] (Fig. 1 a).

Using ensembles of NV-centers, it is possible to perform highly sensitive magnetic imaging using wide-field (e.g., epifluorescence) optical microscopy. In such a case, a thin layer of NV centers is typically engineered close to the surface of a diamond crystal. This layer is then used for two-dimensional mapping of the magnetic field generated by a sample proximal to the diamond’s surface, by projecting the NV-fluorescence onto a camera sensor and performing ODMR measurements [125]. As such, sub-micrometer-resolved magnetic-field maps can be achieved using high magnification and high numerical-aperture (NA) microscopes equipped with, for example, a common charged-coupled device (CCD)/complementary metal-oxide-semiconductor (CMOS) camera. Furthermore, NV centers are oriented along one of four crystallographic $\langle 111 \rangle$ directions within the diamond crystal lattice (in particular along the $\langle 111 \rangle$, $\langle 1\bar{1}1 \rangle$, $\langle 11\bar{1} \rangle$, and $\langle \bar{1}11 \rangle$ crystal axes; see inset Fig. 3.4.2). A diamond crystal hosting an ensemble of NV centers typically contains an equal number of NVs for each direction. As such, ODMR spectra from all NV orientations yield the necessary information to reconstruct vector magnetic field components from magnetized structures proximal to the NV centers. Wide-field NV-based imaging techniques have already been used to image magnetic fields generated by magnetic thin films [17], nanoparticles [126], vortices in type-II superconductors [127], and even to reconstruct the current flow inside integrated circuits [128] or graphene

field-effect transistors [129].

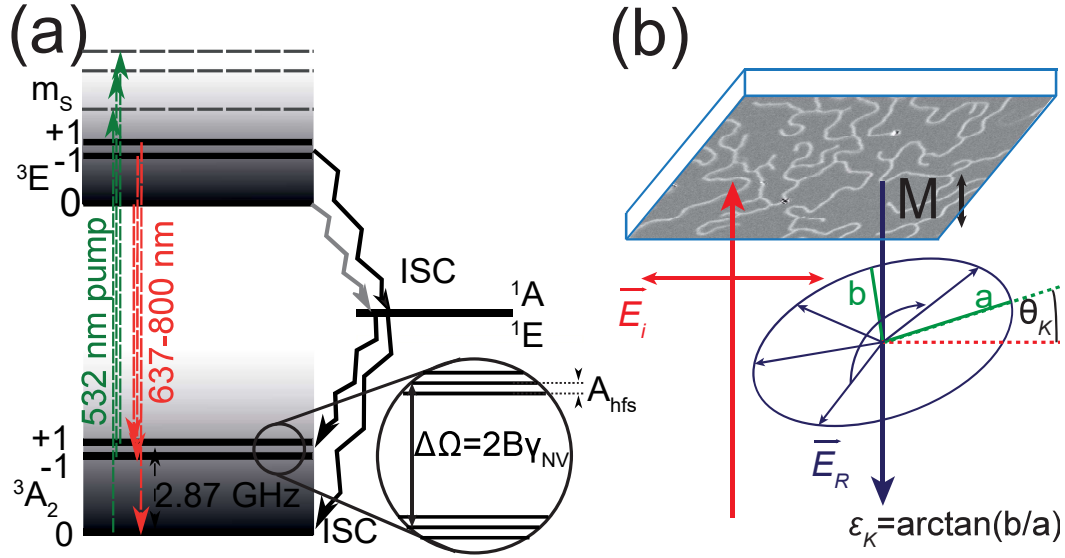


Figure 3.3.1: (a) NV-energy-level diagram (b) Schematic of the polar MOKE. \vec{E}_i describes the linearly polarized incident light and \vec{E}_R the reflected light with rotation angle Θ_K and ellipticity ϵ_K .

3.3.2 Magneto-optical imaging

Magneto-optical effects from magnetized media can be observed via transmission- or reflection-based measurements. The optical effects that manifest themselves when light is reflected from the surface of a magnetized material are conventionally designated as MOKE. MOKE microscopy, i.e. a technique capable of studying MOKE with the use of an optical microscope, is one of the most prominent tools for the spatio-temporal visualization of distributions of magnetization (\mathbf{M}) within magnetic materials [123]. In general, Kerr effects manifest as changes of the intensity and/or the plane of polarization (Θ_K) and the ellipticity (ϵ_K) of an incident linearly polarized light upon reflection. All different types of Kerr effects (polar, longitudinal, transverse) mostly scale linearly with magnetization (higher order, quadratic, effects can also be observed using MOKE

microscopy [123]; in this work we will focus on samples that show no quadratic MOKE and for this reason we will assume MOKE to be linear in a sample's magnetization). As such, investigation of the magnetization of a magnetic sample becomes possible with the use of a simple optical microscope that consists of a polarization selection and a polarization analysis step. For most cases of interest, as in our work here, the polar type of MOKE is typically studied, which means that one senses the magnetization component perpendicular to the sample's surface (Fig. 3.3.1 (b)). Moreover, the polar MOKE manifests as a change both in polarization angle (Θ_K) and ellipticity (ε_K), while the reflected intensity remains unchanged.

3.3.3 Combined MOKE/magnetic imaging microscopy

Combination of both imaging modalities, NV-based magnetic and MOKE, is possible by the additional incorporation of polarization-sensitive preparation and analysis steps in the optical setup required to perform NV-based magnetic imaging. In particular, by pre-selecting the polarization state of the optical excitation required for the NV-based magnetometric protocol (i.e., green laser light), and imaging changes in its polarization state upon reflection from a magnetized sample placed upon the diamond crystal, while simultaneously imaging the NV-fluorescence, one obtains a combined image of magnetization and their resulting magnetic fields.

3.4 Experimental Methods

3.4.1 Magnetic sample

To demonstrate the capabilities of an imaging setup that can perform measurements of magnetization and magnetic fields, we use a multilayered ferromagnetic structure that shows rich topological magnetic structures (magnetic domains) under the influence of external magnetic fields.

The sample is a Ta(5 nm)/Co₂₀Fe₆₀B₂₀(1 nm)/ Ta(0.08 nm)/MgO(2 nm)/Ta(5 nm) material stack that is grown on a Si/SiO₂ substrate (500 μ m thickness) by DC

magnetron sputtering. The use of a Singulus Rotaris sputtering system allows us to tune the thickness of the layers with high accuracy (reproducibility better than 0.01 nm) [130]. The Ta(0.08 nm) insertion layer, that is not even a complete Ta monolayer, is inserted to fine tune the perpendicular (out-of-plane) magnetic anisotropy (see inset Fig. 3.4.2 left side) stemming from the $\text{Co}_{20}\text{Fe}_{60}\text{B}_{20}/\text{MgO}$ interface [131]. This allows us to get closer to the spin reorientation transition [132]. Thereby, we can achieve a typical hour-glass shaped hysteresis loop indicating the presence of magnetic domains or a skyrmion phase [133]. Using SQUID-based measurements, we determine the saturation magnetization of the sample to be $M_s \approx 760 \text{ kA/m}$ at room temperature.

3.4.2 Experimental setup

Optical Setup - In Fig. 3.4.2 we present the experimental setup we use for combined magnetic field (NV) and magnetization (MOKE) measurements. The basis of the setup is a home-built inverted epifluorescence microscope.

As light source for both the magnetometric protocol and the light-polarization measurements, we use a 532 nm diode laser (Laser Quantum, Gem 532 nm). The laser intensity is stabilized with a feedback system using an acousto-optical modulator (AOM, ISOMET-1260C with an ISOMET 630C-350 driver) controlled with a proportional-integral-derivative controller (PID, SRS SIM960). The excitation and reflected/PL beams are split using a 50:50 beam splitter cube (BSC) before the objective. To operate in wide-field configuration another lens ($f=150 \text{ mm}$) is placed before BSC which leads to an enlarged excitation area.

The imaging system consists of an air objective (Olympus UplanFL N 60X) with magnification of $60\times$, a working distance of 0.2 mm, and a correction collar that allows us to compensate for cover glass thicknesses of 0.11-0.23 mm. As detector, we use a scientific-CMOS (sCMOS) camera (Andor Zyla 5.5) with a pixel area of $6.5 \times 6.5 \text{ }\mu\text{m}^2$. This leads to an effective pixel area of $\approx 108 \times 108 \text{ nm}^2$ in the focal plane, i.e. on the sample. The home-built sample holder consists of a thickness #0 ($\approx 85 - 115 \text{ }\mu\text{m}$) coverslip, which is glued onto a printed

circuit-board that is supported upon a 3D translation stage. The coverslip is electroplated with a copper layer, from which an omega shaped stripline is produced. This stripline is used to deliver the MW fields required for NV-based magnetometry. The FOV is adjusted in such a way that it resides in the center of the omega loop. On top of the coverslip, we place our diamond sensor, and on top of the diamond sensor, the magnetic sample under investigation. The diamond sample is oriented in such a way, that the NV layer is proximal to the magnetic layers of the sample (see inset Fig.3.4.2). To fix the sample-sensor distance to distances ($< 10 \mu\text{m}$), reduce lateral movement and the amount of aberrations, we use microscope immersion oil between the coverslip/diamond and diamond/sample surfaces. A detailed schematic of the diamond sensor and magnetic sample configuration is shown as inset in Fig.3.4.2. The laser beam enters and exits the diamond through the coverslip.

To image the NV PL, we use a 650 nm longpass filter (FEL0650, Thorlabs) to remove the reflected green light. For MOKE imaging, we remove the longpass filter and introduce a neutral density filter (optical density= 3) before the camera. This is done to coarsely match the amount of reflected photons from the green laser beam to the number of detected photons in the observed NV fluorescence (under typical experimental conditions). This facilitates operation (i.e. the use similar acquisition settings), while sacrificing optimal polarimetric sensitivities.

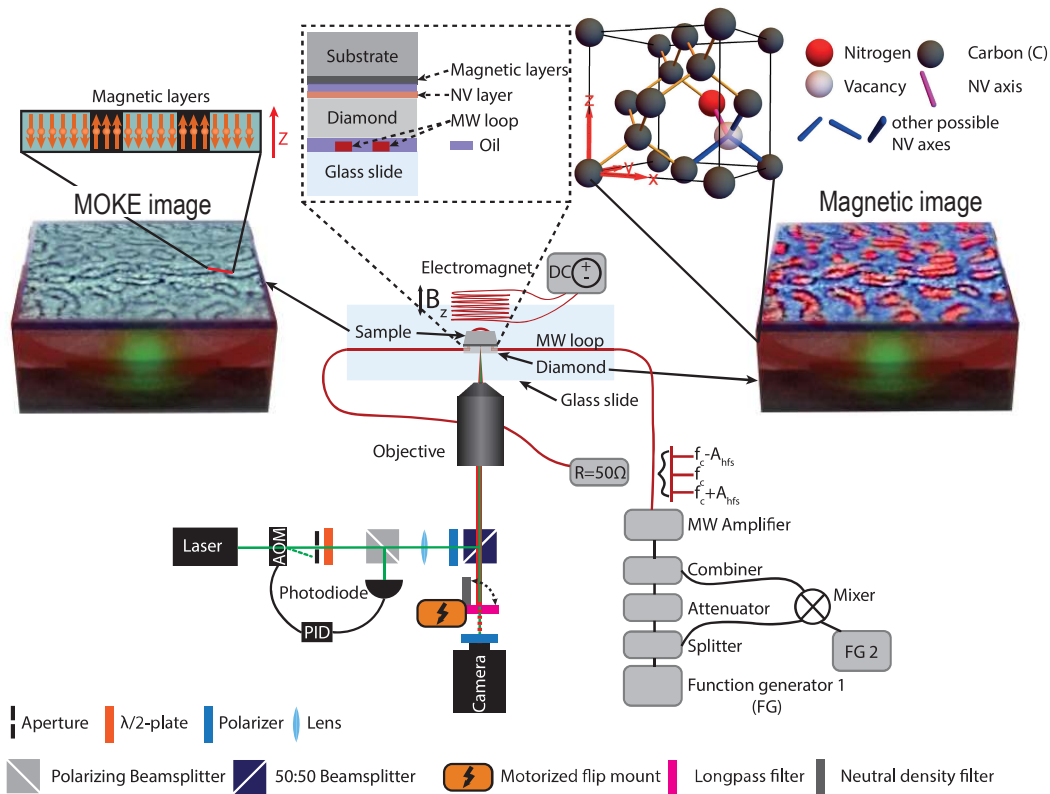


Figure 3.4.2: Schematic of the experimental setup. **Top left:** An example of a MOKE image with the inset depicting a magnetic sample having an out-of-plane anisotropy. **Center:** Experimental arrangement of the diamond sensor and magnetic sample (resting upon a microscope slide). The inset shows a detailed view of the different layers indicating the arrangement of diamond sensor and magnetic sample. **Top right:** Inset showing a unit cell of the diamond lattice containing a single NV center and indicating all other possible NV orientations. **Bottom left:** Optical setup for combined MOKE and NV based imaging. **Bottom right:** MW setup used to drive transitions among the NV center's ground state spin sublevels.

Magnetic Sensor - For wide-field NV magnetic imaging, we use a near-surface, high density NV ensemble. In particular, a 100 nm ^{14}N doped, isotope-purified (99.9% ^{12}C) layer was grown by chemical vapor deposition on an electronic-grade diamond substrate (Element Six). The sample was then implanted with 25 keV He^+ at a dose of 10^{12} ions/cm 2 to form vacancies, followed by a vacuum anneal at 900 °C for 2 hours for NV formation and an anneal in O_2 at 425 °C for 2 hours for charge-state stabilization [51]. The resulting ensemble has an NV density of $\sim 1.2 \times 10^{17}$ cm $^{-3}$. This value was obtained by comparing the fluorescence of the layer to the average of near-surface single NV centers in a control sample. The diamond crystal has dimensions of 2×2 mm 2 and a thickness of $\approx 90 - 100$ μm .

External fields - To generate the magnetic domains in the sample, we apply a bias magnetic field (B_z) with the use of a coil (length 2.8 cm, radius 3 cm, producing approximately ~ 6 G/A). The coil is supplied with DC current using a computer controlled power supply.

To perform the NV-based magnetic imaging, a MW source/function generator (SRS SG384) is used. The MW signal is split and mixed with a 2.16 MHz signal and then combined again, in order to resonantly address and drive all (three) hyperfine-resolved NV spin resonances simultaneously. This allows us to obtain full contrast ODMR spectra without the drawback of power broadening and, thus, yields improved magnetometric sensitivities [134]. All MW frequency components are amplified with a 16 W (+43dB) amplifier (ZHL-16W-43+), and passed through a circulator (Pasternack CS-3.000) and a high-pass filter (Mini Circuits VHP-9R5) before they are transmitted through the omega shaped stripline. A schematic of the setup required to generate the external fields can be seen in Fig. 3.4.2

Polarization control - To perform MOKE imaging in polar configuration, the setup is equipped with two linear polarizers (Thorlabs LPVISA100): one is placed in front of the BSC to prepare the green light with linear polarization (it also enables for optimization of the magnetometric protocol through the appro-

appropriate selection of polarization). The second one, hereafter called the analyzer, is used for analysis of the polarization state of the reflected light beam and is placed directly in front of the camera. The rotation angle of the analyzer with respect to the polarizer was optimized to obtain the best signal-to-noise ratio (SNR) for MOKE measurements. For the present experimental conditions, this optimum was found when the analyzer was nearly crossed with the polarizer.

To allow for switching between magnetic field and magnetization imaging, a computer-controlled flip-mount is positioned in front of the analyzer that allows us to switch from using the longpass filter (and thus performing magnetic field measurements) to using the neutral density filter (allowing for MOKE measurements).

3.4.3 Magnetic imaging

Obtaining quantitative images of the local magnetic field requires acquisition of ODMR spectra for all pixels within the illuminated FOV. Here, we employ a CW technique for NV ODMR-based magnetic imaging, wherein optical NV spin polarization, MW drive, and spin-state readout via the NV PL occur simultaneously. The diamond sensor is continuously illuminated with ≈ 80 mW of 532 nm laser light, and the resulting NV PL is collected with the microscope's objective.

For each frequency point of the NV ODMR spectrum (ν_1), PL images are captured and normalized by images captured at a fixed off-resonant frequency (in our case $\nu_{\text{off}} = 2.16$ GHz). The number of detected photons on each pixel at ν_1 is then divided by the detected photon number at ν_{off} for the same pixel. This sequence is then repeated between 15 and 40 times (for every selected ν_1); a typical exposure time is 100 ms per sequence.

Here, we aim to image fields from a sample with a perpendicular (out-of-plane) magnetic anisotropy. The bias magnetic field required to manipulate samples with this anisotropy is applied along the $\langle 100 \rangle$ axis of the diamond crystal. As such, the applied field and the resulting magnetic fields from the magnetic structure lead to (almost) equal magnetic field projections along all (eight) different

NV orientations (along four axes) in our diamond sample. This can easily be shown by calculating the scalar product between the different possible NV axes ($\langle 111 \rangle$, $\langle 1\bar{1}1 \rangle$, $\langle 11\bar{1} \rangle$, and $\langle \bar{1}11 \rangle$) and the $\langle 100 \rangle$ direction describing the magnetic field. This, in turn, results in degenerate magnetic eigenstates and, thus, equal transition frequencies in addressing NVs along the different axes. In fact, the magnetic stray fields generated by the sample are not exactly oriented along the applied field, but since the splitting created by transverse components is smaller than the linewidth this results only in broadening of the resonances. As mentioned earlier, due to hyperfine interactions this results in two sets of three transition frequencies, which are separated by $2\gamma_{NV}B_{NV}$ ($\gamma_{NV} \approx 28 \text{ MHz/mT}$ and B_{NV} projection of the magnetic field along the NV axis). In order to increase the sensitivity of our sensor, we simultaneously apply three frequency components with a fixed separation of 2.16 MHz, matching the hyperfine splitting of the resonances. This applied frequency triplet is then scanned over the three NV resonances results, thus, in five dips for both $\Delta m_s = \pm 1$ transition families. The relative amplitude ratios between the five observed lorentzian features in the ODMR spectrum are 1:2:3:2:1 (see Fig.3.5.3(c) and Ref. [134]). This is a result of the fact, that at different carrier frequencies one, two or three hyperfine components of the transitions are on resonance with the MW driving fields. For this reason, the observed features in the obtained ODMR spectra are fitted with two sets of five lorentzians. In the general case of an arbitrarily oriented magnetic field, eight sets of five lorentzians are observable. Overall, by determining their frequency separation we can image the local magnetic field perpendicular to the diamond surface. We determine the average magnetometric sensitivity of our current setup to be $\delta B_{NV} \approx 2 \mu\text{T } \mu\text{m}/\sqrt{\text{Hz}}$ within a FOV of approximately $40 \times 40 \mu\text{m}^2$, which is mainly limited by mechanical instabilities of the setup.

3.4.4 MOKE imaging

MOKE images of the sample-magnetization topology are taken in a similar fashion to the magnetic images after switching to MOKE operation by using the flip

mount. This allows for the collection of the green laser light instead of the NV PL.

For a given strength of the externally applied magnetic field required to change the magnetization state of the sample, we obtain a MOKE signal for each pixel by averaging over 50 acquisition cycles of the camera (typical exposure time: 10 ms per cycle). This average is then normalized to an equivalent measurement performed at a reference field $|B_{ref}| > |B_{sat}|$ [i.e., $S_{MOKE} = [N_{ph}(B_z) - N_{ph}(B_{ref})]/N_{ph}(B_{ref})$]. In our case, B_{sat} , the saturation field at which the magnetic sample is in a monodomain state with all the domains/spins aligned with the external magnetic field, is approximately $B_{sat} \approx 1$ mT. This comparison with a reference image allows us to eliminate beam intensity variations in the FOV, the effect of impurities/surface features and birefringence in the diamond crystal. We determine the polarimetric angle-imaging sensitivity of our current setup to be $\delta\Theta_K \approx 50 \mu\text{rad } \mu\text{m}/\sqrt{\text{Hz}}$ (again mainly limited by mechanical instabilities of the setup).

3.5 Results

In Fig. 3.5.3 we show the main result of this work. Figure 3.5.3 (a) shows the hysteresis magnetization curve of our magnetic sample obtained by implementing a MOKE measurement sequence and by averaging over all pixel values within the FOV. For each strength of the externally applied magnetic field (B_z), which is used to generate the magnetization curve [for comparison we also present measurements obtained using a commercial MOKE microscope (Evico GmbH)]. In Fig. 3.5.3 (b) we show a MOKE image of the sample-magnetization topology under an externally applied magnetic field strength of $B_z = 0.329$ mT, demonstrating our ability to observe magnetic (stripe) domains and qualitatively image their magnetization.

In Fig. 3.5.3 (c) we present the magnetic field map generated by the stripe domains as obtained by NV-based magnetic imaging. Using the differences between the resonance frequencies observed in the recorded ODMR spectra, we obtain the

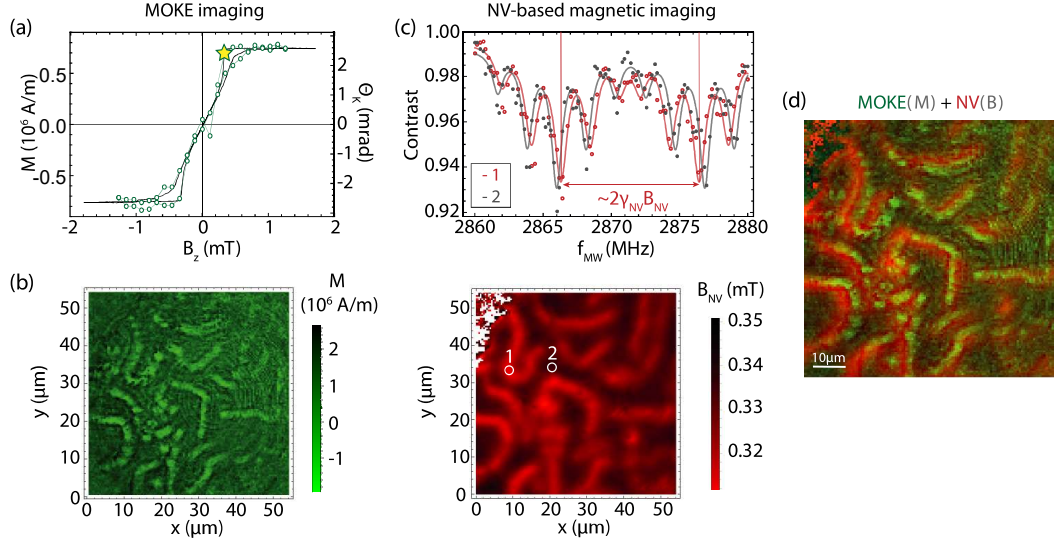


Figure 3.5.3: *Magnetization and magnetic field imaging using MOKE and NV-based magnetic field imaging* - (a) Out-of-plane magnetization curve of the magnetic sample (open green circles), and for comparison we present the magnetization curve obtained using a commercial MOKE microscope (black line). The starred point denotes the position in the hysteresis curve where the MOKE and NV-based magnetic images were obtained. (b) MOKE image for an applied external magnetic field of $B_z = 0.329$ mT. (c) ODMR spectra for two different positions within the imaged field-of-view (points are measured data while the lines represent the best fit for these data sets) and imaging of the resulting magnetic fields generated from the sample for an external field of $B_z = 0.329$ mT (the magnetic field is obtained by fitting the ODMR spectra for each pixel). (d) NV (red) and MOKE (green) images overlapped.

direction (relative to the externally applied magnetic field) and strength of the magnetic field generated by a stripe domain and its surrounding environment, which is $\approx 22 \mu\text{T}$. Particularly, in the top of Fig. 3.5.3 (c), we show ODMR spectra for two specific cases (i.e. imaging pixels): the first one shows the magnetic field originating from the center of a magnetic stripe domain while, the second one, the magnetic field originating from the sample's surface (far away from a stripe domain). The observed ODMR frequency splittings (between the sets of five lorentzians corresponding to the NV $m_s = -1$ and $m_s = +1$ spin states), are reduced for the pixels that image the magnetic fields from the stripe domains

compared to the pixels imaging surfaces without stripe domains; in this case (Fig. 3.5.3 (a), the sample's surface magnetization is aligned with the externally applied magnetic field while within the stripe domains the magnetization is reversed (resulting, thus, in an overall reduced observed magnetic field and, hence, in a reduction in the observed ODMR splittings). We note here that maximum magnetic (stray) field values are attainable at the center of the magnetically imaged stripe domains due to the stand-off distance between the NV layer and the sample's surface ($\approx 3 - 4 \mu\text{m}$) taking into consideration that the magnetic domains have a width of $\sim 3 \mu\text{m}$ (for larger domains, the main magnetic contrast would be expected closer to a domain's observed walls).

It should be noted that the effective bandwidth of each measurement in our imaging configuration is different. While a MOKE image takes $\approx 0.5 \text{ s}$, an NV image (for which, here, we record the full ODMR spectrum) takes $\approx 300 \text{ s}$. The time required to record an NV-based magnetic image could be significantly decreased to $\approx 3 \text{ s}$ by recording magnetic images at a single-frequency and use a calibration (e.g., and image at an off-resonant excitation frequency) to get quantitative information about the magnetic field, but this is beyond the scope of this work.

Finally, in Fig. 3.5.3 (d) we present the MOKE and NV magnetic images overlapped to demonstrate the complementary character of the two imaging modalities, while it also allows us to clearly investigate the differences in the observed sizes of the stripe domains between the two imaging modalities. These differences are related to the offset distance between diamond and magnetic sample ($\approx 3 - 4 \mu\text{m}$) that results in blurring of the observed features in the (NV) magnetic image. This also verifies that the resolution of the NV magnetic image is currently determined by the size of this offset distance and not by the optical resolution of the microscope. We also note here that this becomes consequential when the stripe domains are dense, i.e. when the distance between the stripe domains is smaller than the resolution of NV-magnetic imaging, resulting in noticeable differences between the NV-magnetic and MOKE images. In such cases,

the magnetic fields from different domains might, for example, add up and it will not be easily possible to reconstruct the magnetic topology of the domain structure. However, such an issue can be resolved (in future implementations) by minimizing the distance between the diamond surface and the magnetic sample [for instance, one way to minimize this gap is to directly deposit (2D) magnetic materials onto the diamond surface [135]]. Furthermore, we observe in our images slight deviations from perfect overlap between the observed magnetization and magnetic field maps from stripe features that reside at the edges of our FOV. We believe this is the result of a combination of offset-related magnetic field gradients (of the field generated by the domains) and off-axis aberrations. Further investigations are required to resolve this issue.

3.6 Discussion and Conclusions

We present a platform for wide-field imaging of the magnetization and resulting magnetic fields of magnetic structures using engineered diamond magnetic sensors and an optical setup that allows for both measurement modalities. Our work extends recently developed NV-magnetic imaging techniques used to study magnetic systems by demonstrating how the addition of polarization analysis can incorporate simultaneous information about the magnetization of the sample.

Possible extensions to the current experimental setup are possible for both the MOKE- and NV-based imaging part. The NV-based imaging, for example, can be extended to the zero-field regime by implementing recently developed measurement schemes [136] or even be operated in a MW-free modality [137, 138]. Furthermore, while the setup is currently only sensitive to out-of-plane magnetizations (polar MOKE), it can be extended to measurements of longitudinal and transverse MOKEs, i.e. the measurement of in-plane magnetizations, by illuminating the sample at an angle [123]. To do so, the incorporation of field coils for the generation of in-plane magnetic fields would be necessary. Most importantly, the angled illumination allows for truly concurrent acquisition of NV and MOKE images, as the reflected beam and fluorescence are now detected

in different areas of the camera (or independently imaged from their respective optical paths).

Magnetic structures, and generally correlated and topological electron systems, present crucial technological opportunities for information storage and computation, and their inherent nonvolatility makes them central to energy-related research and associated technologies. Moreover, our understanding of condensed matter physics is greatly affected by these technologies that exploit the topology of spin structures, as was the case with technologies that exploited the topology of the physical and electronic structure of materials. Our primary goal is to develop an instrument that is ideal for the research and development of these technologies and the study of related emergent phenomena.

3.7 Acknowledgements

This work was supported by the EU FETOPEN Flagship Project ASTERIQS (action 820394), the Dynamics and Topology Centre funded by the State of Rhineland Palatinate, the German Federal Ministry of Education and Research (BMBF) within the Quantumtechnologien program (FKZ 13N14439 and FKZ 13N15064), as well as the German Research Foundation (DFG SFB TRB 173 SPIN+X AOI, 403502522). ■■■■ acknowledges support by the Alexander von Humboldt Foundation. ■■■■■■■■■■ acknowledge support by the UW Molecular Engineering and Materials Center with funding from the NSF MRSEC program (No. DMR-1719797).

4 Magnetic sensing at zero field with a single nitrogen-vacancy center

The following chapter has been, apart from minor formatting and style changes, published as shown below in a peer-review journal. The reference to the published manuscript is:

T. Lenz, [REDACTED]. Magnetic sensing at zero field with a single nitrogen-vacancy center. *Quantum Sci. Technol.*, 6 (034006), 2021

I co-authored this work, contributing in microwave board design (a direct adaptation from [139]) and fabrication, data acquisition, analysis and interpretation, and in preparing the manuscript for publication.

4.1 Abstract

Single nitrogen-vacancy (NV) centers are widely used as nanoscale sensors for magnetic and electric fields, strain and temperature. Nanoscale magnetometry using NV centers allows for example to quantitatively measure local magnetic fields produced by vortices in superconductors, topological spin textures such as skyrmions, as well as to detect nuclear magnetic resonance signals. However, one drawback when used as magnetic field sensor has been that an external bias field is required to perform magnetometry with NV centers. In this work we demonstrate a technique which allows access to a regime where no external bias field is needed. This enables new applications in which this bias field might disturb the system under investigation. Furthermore, we show that our technique is sensitive enough to detect spins outside of the diamond which enables nanoscale zero- to ultralow-field nuclear magnetic resonance.

4.2 Introduction

Single nitrogen-vacancy (NV) centers are widely used as nanoscale sensors for magnetic and electric fields, strain and temperature[36, 37, 64] even under ambient conditions. Here, we demonstrate the application as magnetic field sensor without the use of a bias field i.e. at zero field. Nanoscale magnetometry using NV centers allows one to quantitatively measure local magnetic fields produced by vortices in superconductors [18], topological spin textures such as skyrmions [121], to perform nanoscale nuclear-magnetic-resonance spectroscopy down to the single-molecule level [140], and even to study exotic beyond-the-standard-model interactions [38, 39, 141]. Commonly an axial bias field (along the NV axis) is applied in order to lift the degeneracy of magnetic sublevels in the ground state and gain first-order sensitivity to magnetic fields. In some applications, such as for example zero- to ultralow-field (ZULF) nuclear magnetic resonance (NMR) spectroscopy [142] or the study of ferromagnetic thin films [143], the bias field significantly disturbs the sample under investigation perturbing or even disrupting the measurement. In this work, building on the works of other authors near zero bias-field [144][145], we demonstrate a method to extend the range of application of single NV center based magnetometry to this regime. We use circularly polarized microwave (MW) fields, similar to work performed on an NV center ensemble [136]. The NV center in diamond consists of a substitutional nitrogen atom and a neighbouring empty site in the diamond lattice. Sensing is performed with negatively charged NV centers, where an additional electron is obtained from a donor within the diamond. A simplified energy-level diagram of NV-ground state is shown in Fig.1a). The NV-center energy levels close to zero ambient field are described by the following Hamiltonian [56, 60, 146].

$$\begin{aligned} \mathcal{H}/h = & (D_0 + \Pi_z)S_z^2 + \gamma_{NV}\mathbf{B} \cdot \mathbf{S} + \Pi_x(S_y^2 - S_x^2) \\ & - \Pi_y(S_xS_y + S_yS_x) + A_{HF}S_zI_z + Q[I_z^2 - I(I+1)/3], \end{aligned} \quad (14)$$

where h is Planck's constant, $\gamma_{NV} = 28$ GHz/T the electron gyromagnetic ratio, \mathbf{B} the magnetic field vector, \mathbf{S} the electronic spin vector with its components

S_x, S_y, S_z , respectively, and $D_0 \approx 2.87$ GHz the axial zero field splitting. \mathbf{I} with components I_x, I_y, I_z is the nuclear spin vector of the intrinsic ^{14}N nucleus with the axial hyperfine coupling parameter $A_{HF} = -2.16$ MHz and quadrupolar coupling Q . Π_x, Π_y, Π_z describe the effective field acting on the NV center, which consists of strain and local electric field. The coordinate system is chosen such that the z axis is parallel to the NV axis. For simplicity and without loss of generality we assume $\Pi_z = 0$ for the scope of this work. In addition, note that the quadrupolar interaction between the ^{14}N nucleus and the electron spin does not have an influence on the electronic transition frequencies as they are nuclear spin conserving (Fig.4.2.1a right).

In most NV-magnetometry experiments a bias magnetic field is such that $|\gamma_{NV}B_z| > |\Pi_x|, |\Pi_y|, |A_{HF}|$ and $|B_x|, |B_y| \ll |D_0/\gamma_{NV}|$. In good-quality diamond samples $|A_{HF}| > |\Pi_x|, |\Pi_y|$ is also achieved and enables to resolve the hyperfine structure of the NV center, which is essential for the presented method. The hyperfine coupling to the internal nitrogen spin leads to an energy-level structure shown in Fig.4.2.1a. The left side shows the simplified energy levels when omitting the last term in eq.15, which then allows for the measurement of the magnetic field by measuring the splitting between the $m_s = \pm 1$ states. This spectrum with only two resonances increases in complexity, when the nuclear spin of the nitrogen host is taken into account (last term in eq.15 and right side Fig.4.2.1a). Here it is shown for the case of a ^{14}N nucleus with spin=1 (99.6% natural abundance). This means that there are three possible projections ($m_I = 0, \pm 1$) along the NV axis, which results in three resonances with a separation of A_{HF} . The frequency difference of the central resonances of the two triplets is still $2\gamma_{NV}B_z$ (as shown on the right of Fig.1a). The transition frequencies of the triplets cross at $\gamma_{NV}|B_z| = |A_{HF}|, |A_{HF}|/2, 0$. At $B_z = 0$ all three transition frequencies of the two sets cross (see also Fig.4.4.3a). In addition, due to the effective fields Π_x, Π_y , the $m_S = \pm 1$ states do not remain eigenstates for the $|m_I = 0\rangle$ states and a level anticrossing occurs. Both, crossing and anticrossings occurring at $B_z = 0$ result in difficulties for magnetometry

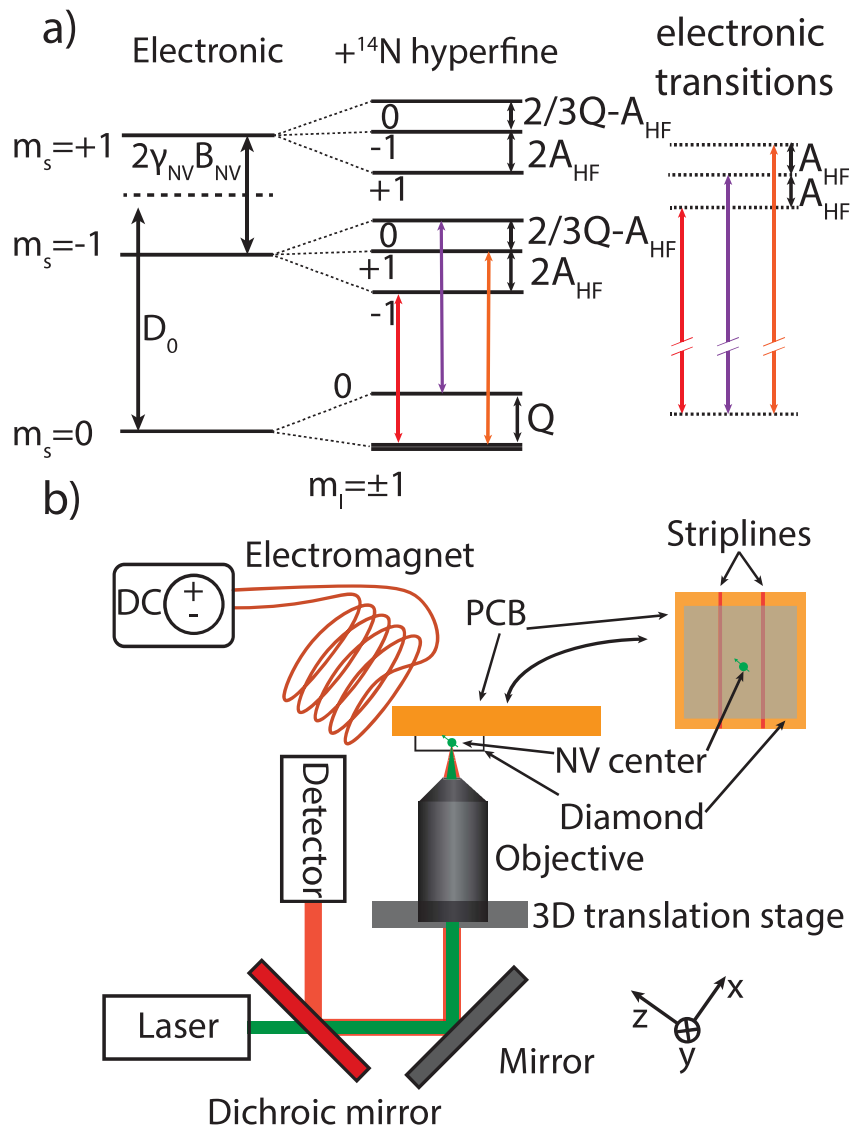


Figure 4.2.1: (a) Energy-level diagram of the NV center ground state without hyperfine interactions (left), which get split due to hyperfine interaction with the ^{14}N host nucleus (center), and a representation of the resulting allowed electronic transitions (right) b) Schematic of the experimental setup.

at $|B_z| < \Delta\nu/(2\gamma_{NV})$ where $\Delta\nu$ is the observed linewidth. In this regime, shifts of the transition frequencies which are proportional to magnetic field changes cannot be resolved anymore or as for the case of an anticrossing (of states with equal I_z) the proportionality to magnetic is lost. In this work, we present a robust solution to this issue with the use of circularly polarized microwaves in the magnetometry protocol. Circularly polarized MWs allow us to exclusively drive transitions with $\Delta m_s = \pm 1$. This leads to a single set of three resonances without crossings and therefore a linear relation to magnetic field even at zero magnetic field. For a single NV center with the ^{14}N nucleus in a fixed eigenstate, one would expect a single resonance for each of the two $\Delta m_s = \pm 1$ transitions. However, two distinct sets of three resonances are observed as a result of the fact that the ^{14}N spin flips several times within our measurement. The ^{14}N basically acts as a source for a local bias field for the NV-electron system, where the value of the bias field depends on the nitrogen nuclear spin state. Due to the fact that the longitudinal relaxation time (T_1) for the ^{14}N spin at room temperature is way below 10 ms [147], within a single measurement sequence (here: ODMR or Ramsey), the nuclear spin remains fixed, whereas over the time of the whole measurement one already observes an averaging over all three orientations of the nuclear spin, resulting in the sets of three resonances. We remark that, if one were able to fix the ^{14}N nuclear spin in one of the $m_I = \pm 1$ states, circularly polarized MW fields would have been unnecessary since the local bias would lift the degeneracy. Since this is not the case, we use circularly polarized MW fields to overcome this issue.

4.3 Experimental setup

In Fig. 4.2.1b a schematic of our experimental setup is shown. It consists of a home-built confocal microscope with a high numerical aperture oil-immersion objective (Olympus UPLSAPO 60XO). The diamond sample containing single NV centers is mounted on a printed circuit board (PCB) which is used to apply circularly polarized MW fields to drive the transitions in the NV-center ground

state. The design of the PCB follows earlier works [136, 139] and mainly consists of two parallel striplines, which are separated by 0.6 mm (see Fig. 4.2.1b). This allows us to create circularly rotating magnetic fields in the center between the striplines and at 0.3 mm (=thickness of the diamond crystal) distance from the PCB. The microwave pulses for spin manipulation were synthesized with an Arbitrary Waveform Generator (AWG; Tektronix AWG70002A), that operates at 50 GS/s. The microwave pulses (with adjustable relative phase) from the two output channels of the AWG were independently amplified and fed-into the leads of the micro-circuit for producing circularly polarized microwave excitation. For these experiments we used a single native ^{14}N -containing NV defect in an electronic grade [100] oriented diamond grown via chemical vapour deposition (CVD) from Element six with 100 surfaces. Furthermore, a coil is placed such that it exerts a controllable axial magnetic field to the NV center.

4.4 Results

4.4.1 Characterization of the microwave polarization

First, a single NV center with proper alignment with respect to the microwave striplines needs to be identified. This is done in a two-step process. First, to study NV in the correct position with respect to striplines, the scanning range of our confocal microscope is manually adjusted such that it is centered in the center between the two striplines. The correct height above the board is achieved by selecting NV centers close to the diamond surface which is closest to the objective. In the second step the correct NV orientation in the crystal needs to be selected/identified. This was done by placing a permanent magnet at an angle of $\approx 54^\circ$ with respect to the diamond surface and parallel to the MW striplines. Like this, the NV centers aligned with the magnetic field are also in the right orientation in order to apply circularly polarized MWs. After a single NV center aligned with the permanent magnet was identified ($B_z \approx 450 \mu\text{T}$), we performed Rabi-oscillation experiments on both the $\Delta m_s = +1$ and $\Delta m_s = -1$ transitions while sweeping the relative phase between the MWs

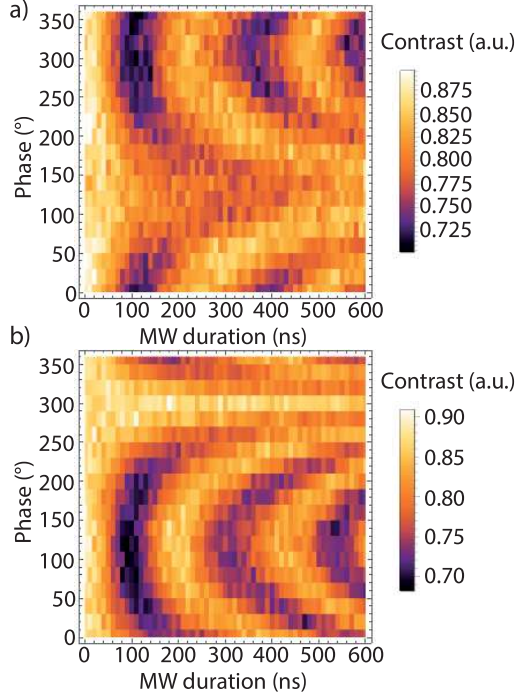


Figure 4.4.2: Rabi measurements performed to determine the driving strengths of the $\Delta m_s = -1$ (a) and $\Delta m_s = +1$ (b) transitions as a function of the relative phase of the MW fields. The measurements are performed at an axial bias field of $\approx 450 \mu\text{T}$.

applied to the striplines. Figure 4.4.2a shows the $\Delta m_s = -1$ transition with a resonance frequency of 2859 MHz and b the $\Delta m_s = +1$ transition with a resonance frequency of 2882 MHz. One can observe that both respective Rabi frequencies vary strongly upon change in relative phase between the striplines. This is attributed to different MW polarizations resulting from the different phases between the two striplines. For the $\Delta m_s = +1$ transition the Rabi frequency varies between 4.3 and 1.45 MHz and for $\Delta m_s = -1$ between 4.8 and < 0.8 MHz.

From these values, we calculate the purity p of the MW polarization defined as $p = \frac{\Omega_+ - \Omega_-}{\Omega_+ + \Omega_-}$. Ω_+ and Ω_- are the respective Rabi frequencies of the $\Delta m_s = +1$ or $\Delta m_s = -1$ transitions. We obtain $p > 71\%$ in this configuration. Note that

the lower limit is given by the Rabi measurement obtained at a phase difference of 260° while at 300° the Rabi contrast in Fig. 4.4.2b almost vanishes, which indicated that the maximum obtained purity of the circular polarization is significantly higher. It should be noted that the fact that the respective maximum Rabi frequencies are not at $\pm 90^\circ$ is a result of different cable length between AWG and stripline. The asymmetry (e.g. not exactly 180° between the maxima/minima) and imperfect circularity of the MW polarization may arise from imperfect alignment of the striplines with respect to the NV center and was observed in earlier works with this stripline configuration [139]. Even though the polarization is not perfect, it is sufficient for our goals as we demonstrate in the following. In fact, it should be noted that any amplitude imbalance between $\Delta m_s = \pm 1$ transitions leads to a non-zero sensitivity at zero bias field, approaching the same sensitivity as with an applied bias field, as one of the transitions vanishes.

4.4.2 Pulsed optically detected magnetic resonance

After characterizing the MW polarization the permanent magnet is replaced with an electromagnet using the same configuration with respect to the diamond and striplines (see Fig. 4.2.1b). Then axial field sweeps from -200 to $130 \mu\text{T}$ are performed using the electromagnet. Figure 4.4.3a shows a density plot of the resulting pulsed optically detected magnetic resonance (ODMR) traces for linearly polarized microwaves. Note that the MW duration for each MW polarization is matched to a π -pulse when on resonance with the respective transition. At the bottom, i.e. at a field $|\gamma_{NV}B_z| > |A_{HF}|$ the two sets of three hyperfine resonances are well separated. When decreasing the applied bias field one can observe the above-mentioned line-crossings in the ODMR spectra. Especially at zero axial field (indicated by the red line) one observes three transition-frequency crossings. To be more precise, two crossings, while the central one is actually an avoided crossing due to the coupling of the two energy levels via electric fields

and/or strain[148]. In our case, this is characterized by lower contrast (also observable at $\approx \pm 75 \mu\text{T}$). In Fig. 4.4.3b, c the (anti-)crossings are not clearly observable anymore but when analyzing the individual ODMR we could still see the expected reduced contrast for the central resonance at zero field.

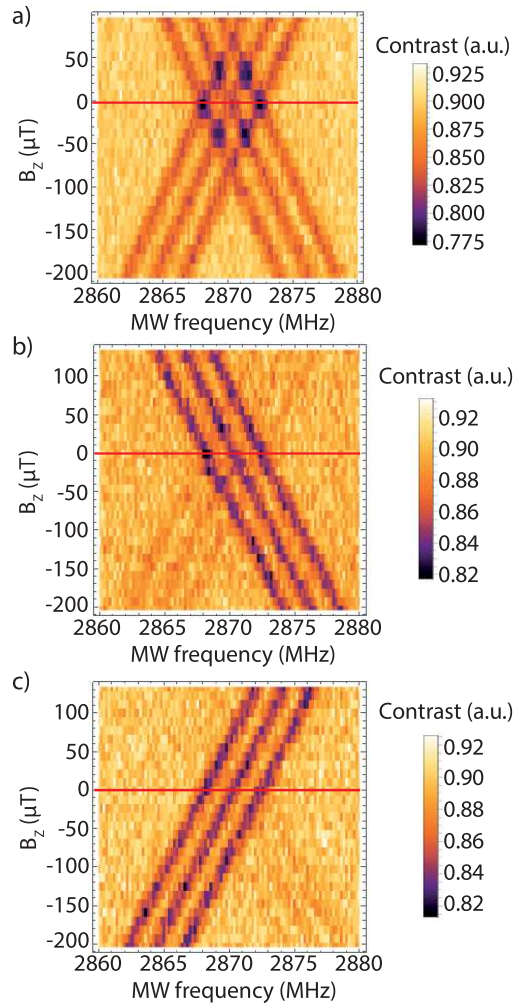


Figure 4.4.3: ODMR spectra for different MW polarizations while sweeping the axial magnetic field using an electromagnet. a) ODMR signal obtained with linearly polarized MW b) σ^+ polarization and c) σ^- polarization.

Figure 4.4.3b shows the case for the $\Delta m_s = +1$ transitions, while Fig. 4.4.3c

shows a field scan for $\Delta m_s = -1$ transitions. The suppressed transitions are still slightly visible, but since they are strongly suppressed, they do not play a role when it comes to determining the transition frequencies of the strongly driven transition even at zero field. This shows already that magnetometry including advanced pulse sequences can also be applied at zero field if circularly polarized MW are used.

4.4.3 Ramsey sequence

To enhance the magnetic sensitivity and in preparation for a future application of this technique in sensing low-frequency magnetic fields, we employ a Ramsey scheme[71]. The frequency of the central anticrossing (2.87 GHz) in Fig. 4.4.3a was chosen as driving frequency and the magnetic field was swept around zero axial field. In addition to that, the phase of the readout $\pi/2$ pulse was dynamically modified (depending on τ) to implement a shift of the observed signals from DC to ≈ 10 MHz. In Fig. 4.4.4 the results of a Fourier transform of the initial Ramsey time trace is shown. One can clearly observe the same contrast over the full range of axial magnetic fields, which again proves that we preserve the same magnetic sensitivity while crossing zero magnetic field. In addition to the ^{14}N hyperfine splitting, we see hints of an underlying splitting induced by a nearby ^{13}C nucleus in the Fourier-transformed signal, which is not fully resolved due to limited coherence time of our sensor spin. But this also demonstrates the robustness of this technique: even in the presence of additional couplings to different nearby nuclear spins, magnetometry around zero field can be pursued.

To estimate the sensitivity of the technique, we determine the photon shot-noise limited sensitivity η of a Ramsey measurement that is given by:

$$\eta = \frac{\hbar}{g \mu_B C} \frac{1}{\sqrt{I_0 t_L / t_{seq} T_2^*}} \quad (15)$$

with I_0 being the detected photoluminescence rate, t_L the duration of the readout laser pulse, t_{seq} the total sequence length and T_2^* the coherence time of the NV center. Using common parameters used in our experiment, for this diamond

sample where the coherence time is $\approx 3\mu\text{s}$, this results in a projected shot-noise limited sensitivity of approximately $350\text{ nT}/\sqrt{\text{Hz}}$, which is a typical value for a diamond of this type [64]. This is sufficient to measure signals of, for example, proton spins [29] or other nuclear spins on the diamond surface or to study (anti-)ferromagnets using a shallow NV center and therefore this technique opens the field to the study of the above mentioned systems using NV-center magnetometry at zero field.

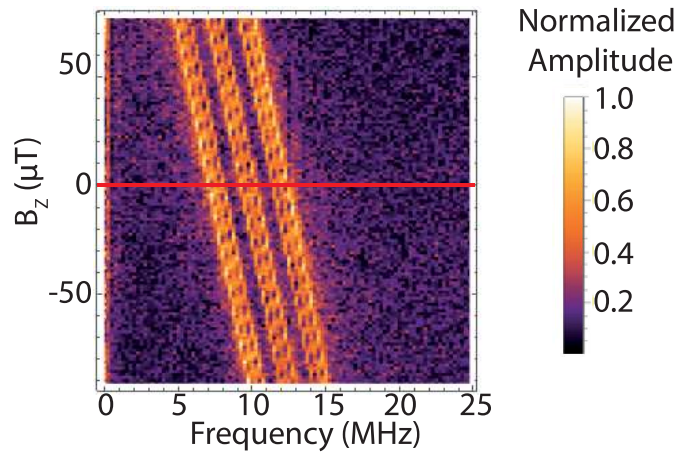


Figure 4.4.4: Fourier transform of the signal obtained from Ramsey experiments performed using σ^+ polarized MW while scanning the axial magnetic field; the signal is effectively detuned by 10 MHz due to the relative phase shifts of the two $\pi/2$ pulses.

4.5 Other possible approaches to magnetometry with NV centers at zero field

As mentioned above, one could also use a static local bias field instead of a flipping bias ($^{14}\text{N}, ^{15}\text{N}$) which would in turn avoid the need of specifically designed MW structures to produce circularly polarized MWs. A promising candidate for this is an axial ^{13}C nucleus, which can, depending on the exact location, have flipping rates well below 10^{-4} Hz or in an ideal case even zero. As a result both sets of resonances would be separated by the hyperfine splitting of the ^{13}C nucleus and would change in frequency according to the Zeeman effect. A

drawback to this method would be the need for an axial ^{13}C which are usually randomly distributed with an abundance of 1.1% for natural-abundance diamonds. Moreover, the splitting produced by axial carbon is usually on the order of ≈ 70 kHz which requires long NV coherence times to be resolved. Another option would be to initialize the nitrogen spin before each measurement into one of the $m_I = \pm 1$ states, but common methods require a lifted of degeneracy between the m_s states to function, which is not the case at zero field [149]. Additionally, a method using RF fields (\approx MHz, [150]) demonstrated magnetic sensitivity of a NV ensemble in a field regime between zero and ≈ 1 mT. However, this method requires a calibration to retrieve quantitative information and has the drawback of limited working conditions, while our scheme works in arbitrary fields (including zero). This is particularly important in the study of (ferro-)magnetic thin films, where the evolution of spin textures over the full magnetic hysteresis (including at zero) is of interest. For these reasons we focus on the approach with circular MW fields in this work.

4.6 Summary and Outlook

In summary, this paper presents a novel method to utilize NV centers as magnetic field sensors down to zero external magnetic field. This opens the road for applications in which magnetic fields perturb the system such as, for example, nuclear magnetic resonance and (anti-)ferromagnets. We also estimated that the sensitivity of this technique is sufficient to probe statistically polarized nuclear spins on the diamond surface at zero field. In combination with high-resolution sensing techniques such as those developed for high-frequency sensing [151, 152], this technique may open new pathways towards nanoscale ZULF NMR for chemical analysis of liquids and solids down to the single molecule level [153]. Further improvements of the sensitivity of this technique are expected in the case of a [110]-oriented diamond crystal and the use of NV centers with ^{15}N host nuclei. Using a [110]-oriented diamond would allow for improved purity of the MW polarization (up to 100%) with the same double stripline configuration

5 Conclusion and outlook

In summary, this thesis presented the basics of magnetometry with NV centers in diamond. In the beginning, the structure of the NV defect in the diamond lattice was introduced, as well as different methods to artificially create both, (ultrapure) diamonds and NV centers within diamonds. Following up on this, the basic energy-level structure of the NV center was explained with focuses on the optical polarization (initialization) and readout of the NV center's spin state, and on the ground-state Hamiltonian including the magnetically sensitive levels therein. To finalize the introduction, different magnetometry protocols, including pulsed and cw protocols, were introduced and their respective strengths and weaknesses were discussed.

Moreover, chapter 2 of the thesis demonstrated the first NV-widefield observation of vortices in a thin film of the type-II superconductor YBCO. It was shown that by using micron-scale diamonds with a shallow layer of NV centers, it is possible to reduce the distance between SC and NV layers to ≈ 500 nm and therefore allow for the observation of vortices. We performed spatially resolved ODMR measurements to compare the amplitude of the magnetic fields at positions of vortices to the amplitude at positions farther away from the vortices. In addition, a MW field with fixed frequency was applied to increase the imaging speed, while sacrificing the exact quantitative information of the field amplitude. This technique was then used to observe vortices at different cooling fields. By observing the linear relation between the number of vortices and cooling-field strength, it was confirmed that the observed structures were indeed vortices in the superconductor and no other magnetic artifacts.

Due to its versatility, this technique can be used in the future to study a plethora of phenomena in many different superconductors. In particular, NV magnetometry has a high bandwidth up to the GHz regime and would therefore

allow for the detection of dynamics, such as vortex oscillations. Moreover, due to the wide range of operation temperature this technique can be used to study so-called island superconductivity, which is a phenomenon where superconductivity sets in in (small) parts of the SC above the global T_c . This changes the local magnetic properties, while macroscopic properties such as conductivity do not correspond to those of a SC.

The third chapter presented the successful combination of NV magnetic imaging and magneto-optic Kerr-effect imaging in a widefield microscope. To do so, a widefield NV-imaging microscope was additionally equipped with two polarizers and absorption filters on an electrical flip mount. This allowed for automated switching between MOKE and NV imaging. This double purpose microscope was then used to observe magnetic domains in a ferromagnetic thin film. The domains were observed in both the MOKE images as well as the magnetic images obtained by NV imaging, and the images of both techniques were in good agreement.

Future works here focus on reduction of the remaining offset distance between NV and sample, and on the implementation of vector-magnetometry protocols. One possible pathway to achieve a reduction of the offset distance is to use micron-sized thin diamonds as in chapter 2. To extend to vector magnetometry, one straightforward solution for samples with strong out-of-plane anisotropy (as the sample studied in chapter 3), is to use a specifically cut diamond plate. This allows to split the different NV axes with a bias field that is parallel to the planes of the diamond and the magnetic sample and therefore does not affect the magnetic sample (with strong out-of-plane anisotropy). Both of these improvements could lead to the ability to analyze domain walls in more detail, e.g. distinguishing Neel and Bloch walls which leads to deeper understanding of the interactions in the magnetic sample. For truly concurrent measurements of magnetization and the generated stray field, the setup could be upgraded by splitting the fluorescence and reflection pathways and either directing the beams

onto two separate cameras or onto different areas of the sensor of the same camera.

Chapter 4 demonstrated a new method that extends the dynamic range of (single-)NV magnetometry to the regime of zero bias field. With the use of circularly polarized MW fields it was possible to selectively drive the $m_s = 0 \rightarrow m_s = +1$ or the $m_s = 0 \rightarrow m_s = -1$ transitions. This allowed for the elimination of the line crossings in the ODMR spectrum at zero field and with that maintain magnetic sensitivity even at zero field.

While improvements on the MW circuit design can lead to higher MW-field amplitudes and with that Rabi frequencies or an increased homogeneity of the circular MW fields over a larger volume, the current design is already sufficient to open the door to new applications. For instance, with this technique it is possible to perform studies similar to the ones in chapter 3 in zero field, which is a specifically interesting regime for many ferromagnetic thin films and also for magnetic structures such as skyrmions. Another application of particular interest to our group is ZULF NMR, where any (dc-) bias field disturbs the measured system. Using single NV centers here would allow for chemical analysis of a small number of molecules down to single molecules, without the need for a magnetic field for either polarization or detection.

To conclude, this thesis showcases numerous applications of NV magnetometry, as well as new techniques/methods that make these applications possible or extend the applicability of NV-center magnetometry to new regimes and research fields. With this it was demonstrated, that NV magnetometry can be a useful tool to complement and excel different (potentially more sensitive) magnetometer types in several applications due to their remarkable characteristics.

6 Acknowledgements

After years of work on my PhD itself and the studies leading here, there are many people I would like to thank for their support. I would like to start, by thanking my supervisor [REDACTED] for the opportunity to do my PhD research in his group on a variety of interesting projects within the field of NV research and for always being available in case of questions etc. I am very grateful that I was able to meet and work with many different personalities during my PhD, which shaped me as scientist and person and I will use the following paragraphs to thank them.

After that I would like to thank two post-docs within the [REDACTED], namely [REDACTED] for additional supervision. It was a true pleasure working with you and learning from you as experienced scientists different approaches to the many tasks that come up during a PhD and that always had an open ear for me. Thank you also to [REDACTED] who guided me on NMR related issues and was always ready to help out when question arose. Next I would like to thank the NV subgroup, namely [REDACTED] for filling me in nicely into the subject of NV magnetometry, working successfully together on different projects and countless small discussions between doorsteps that made me deepen my understanding of NVs. I would also like to thank the newer members and interns of the NV team, [REDACTED] and [REDACTED] for bringing in some more fresh motivation and enriching the work with new skills and viewpoints.

I would like to thank my colleagues [REDACTED], [REDACTED] for being great company on the bike and special thanks to [REDACTED] who brought me into triathlon and cycling. Another special thanks to my office mate [REDACTED] for correcting my written (and spoken) English whenever necessary and introducing me to the thanksgiving dinner tradition. Moreover I would like to thank all my colleagues in the [REDACTED]

group of whom I consider many my friends today, for making my PhD an overall enjoyable experience and making the HIM a place I enjoyed going to.

Thank you to all my collaborators that I had the pleasure to work with during the last 5 years. Starting from the group of at the Ben Gurion University of the Negev in Be'er Sheeva, Israel. In particular I would like to thank for giving me the opportunity for several internships/visits of his group and labs and supervision. Thank you to , whom I spend numerous hours with in the lab looking for vortices in superconductors and in the end observing them. Thank you to for always helping out inside and outside the lab, taking care that I was never getting bored and experience Israel.

Another group that I am grateful to be able to work with and pay a visit is the group of at Basel University. In particular, apart from thanks to his (former) PhD students and for the collaboration on the vortex imaging project and the diamond fabrication for that and future projects.

Thank you to and his group at Leipzig University, specifically which helped us with the ion implantation of several samples and gave us the opportunity to participate in the implantation itself.

I would like to thank for his hospitality and the opportunity to learn from him and to work in his lab with him together on the subject of zero field magnetometry with NV centers.

Thanks to and his group for being supportive on many different fronts including advise and support for the design of our single NV setup in Mainz over the implementation of an experimental control software and other preliminary joint experiments and the implantation and annealing of diamond samples. By name I would like to mention

Thank you to and his group, in particular

████████████████████ for providing different samples, characterization and fruitful discussions in the scope of the combined MOKE and NV microscope project. Additional thanks to ██████████ for the transfer of hBN onto different diamond samples.

Thanks to ██████████ for setting up the microscope for NV-MOKE imaging and further fruitful discussions during the project.

Thank you to ██████████ and her student ██████████ for the collaborative work and thanks to ██████████ for fabrication of the diamond sample used for NV imaging.

Apart from that I would like to thank also all my friends outside the field of science, which kept my mood and motivation up even when things seemed a bit difficult. Special mention here to the therapeutic "Doppelkopf" sessions with my old school mates ██████████
██████████

Last but not at all least I would like to thank my parents and family for endless support in everything I set my mind on., or when I stuck somewhere. Without you I would not be were I am now, so thanks for everything!

7 Bibliography

References

- [1] H. B. Dang, A. C. Maloof, and M. V. Romalis. Ultrahigh sensitivity magnetic field and magnetization measurements with an atomic magnetometer. *Appl. Phys. Lett.*, 97(151110), 2010.
- [2] J.-H. Storm, Peter Hömmen, Dietmar Drung, and Rainer Körber. An ultra-sensitive and wideband magnetometer based on a superconducting quantum interference device. *Appl. Phys. Lett.*, 110(072603), 2017.
- [3] M. C. D. Tayler, T. Theis, T. F. Sjolander, J. W. Blanchard, A. Kentner, S. Pustelny, A. Pines, and D. Budker. Invited review article: Instrumentation for nuclear magnetic resonance in zero and ultralow magnetic field. *Review of Scientific Instruments*, 88(091101), 2017.
- [4] T. Sander, A. Jodko-Władzińska, S. Hartwig, R. Brühl, and T. Middelman. Optically pumped magnetometers enable a new level of biomagnetic measurements. *Advanced Optical Technologies*, 9(5):247–251, 2020.
- [5] M. I. Faley, J. Dammers, Y. V. Maslennikov, J. F. Schneiderman, D. Winkler, V. P. Koshelets, N. J. Shah, and R. E. Dunin-Borokowski. High- t_c squid biomagnetometers. *Supercond. Sci. Technol.*, 30(083001), 2017.
- [6] D. Budker and D. F. Jackson Kimball, editors. *Optical Magnetometry*. Cambridge University Press, 2013.
- [7] A. Waxman, Y. Schlüssel, D. Groswasser, V. M. Acosta, L.-S. Bouchard, D. Budker, and R. Folman. Diamond magnetometry of superconducting thin films. *Phys. Rev. B*, 89(054509):054509, 2014.
- [8] E. Schaefer-Nolte, F. Reinhard, M. Ternes, J. Wrachtrup, and K. Kern. A diamond-based scanning probe spin sensor operating at low temperature in ultra-high vacuum. *Rev. Sci. Instrum.*, 85, 2014.

- [9] D. M. Toyli, D. J. Christle, A. Alkauskas, B. B Buckley, C. G. Van de Walle, and D. D. Awschalom. Measurement and control of single nitrogen-vacancy center spins above 600k. *Phys. Rev. X*, 2(031001), 2012.
- [10] M. W. Doherty, V. V. Struzhkin, D. A. Simpson, L. P. McGuinness, Y. Meng, A. Stacey, T. J. Karle, R. J. Hemley, N. B. Manson, L. C. L. Hollenberg, and S. Prawer. Electronic properties and metrology applications of the diamond nv^- center under pressure. *Phys. Rev. Lett.*, 112(047601), 2014.
- [11] G. Balasubramanian, P. Neumann, D. Twitchen, M. Markham, R. Kolesov, N. Mizuochi, J. Isoya, J. Achard, J. Beck, J. Tissler, V. Jacques, P. R. Hemmer, F. Jelezko, and J. Wrachtrup. Ultralong spin coherence time in isotopically engineered diamond. *Nat. Mater.*, 8:383–387, 2009.
- [12] T. Ishikawa, K.-M. C. Fu, C. Santori, V. M. Acosta, R. G. Beausoleil, H. Watanabe, S. Shikata, and K. M. Itoh. Optical and spin coherence properties of nitrogen-vacancy centers placed in a 100 nm thick isotopically purified diamond layer. *Nano Lett.*, 4:2083–2087, 2012.
- [13] G. Chatzidrosos, A. Wickenbrock, L. Bougas, N. Leefer, T. Wu, K. Jensen, Y. Dumeige, and D. Budker. Miniature cavity-enhanced diamond magnetometer. *Phys. Rev. Applied*, 8:044019, Oct 2017.
- [14] T. Wolf, P. Neumann, K. Nakamura, H. Sumiya, T. Ohshima, J. Isoya, and J. Wrachtrup. Subpicotesla diamond magnetometry. *Phys. Rev. X*, 5(041001), 2015.
- [15] T. Lenz, G. Chatzidrosos, Z. Wang, L. Bougas, Y. Dumeige, A. Wickenbrock, N. Kerber, J. Zázvorka, F. Kammerbauer, M. Kläui, Z. Kazi, K.-M. C. Fu, K. M. Itoh, H. Watanabe, and D. Budker. Imaging topological spin structures using light-polarization and magnetic microscopy. *Phys. Rev. Applied*, 15(024040), 2021.

- [16] L. M. Pham, D. Le Sage, P. L. Stanwix, T. K. Yeung, D. Glenn, A. Trifonov, P. Cappellaro, P. R. Hemmer, M. D. Lukin, H. Park, A. Yacoby, and R. L. Walsworth. Magnetic field imaging with nitrogen-vacancy ensembles. *New J. Phys.*, 13(4):045021, apr 2011.
- [17] David A. Simpson, Jean-Philippe Tetienne, Julia M. McCoe, Kumaravelu Ganesan, Liam T. Hall, Steven Petrou, Robert E. Scholten, and Lloyd C. L. Hollenberg. Magneto-optical imaging of thin magnetic films using spins in diamond. *Scientific Reports*, 6(22797), 2016.
- [18] L. Thiel, D. Rohner, M. Ganzhorn, P. Appel, E. Neu, B. Müller, R. Kleiner, D. Koelle, and P. Maletinsky. Quantitative nanoscale vortex imaging using a cryogenic quantum magnetometer. *Nature Nanotechnology*, 2016.
- [19] J.-P. Tetienne, T Hingant, L J Martínez, S Rohart, A Thiaville, L Herrera Diez, K Garcia, J.-P. Adam, J.-V. Kim, J.-F. Roch, I M Miron, G Gaudin, L Vila, B Ocker, D Ravelosona, and V Jacques. The nature of domain walls in ultrathin ferromagnets revealed by scanning nanomagnetometry. *Nature Communications*, 6(1):6733, 2015.
- [20] I. Gross, W. Akhtar, V. Garcia, L. J. Martínez, S. Chouaieb, K. Garcia, C. Carrétéro, A. Barthélémy, P. Appel, P. Maletinsky, J.-V. Kim, J. Y. Chauleau, N. Jaouen, M. Viret, M. Bibes, S. Fusil, and V. Jacques. Real-space imaging of non-collinear antiferromagnetic order with a single-spin magnetometer. *Nature*, 549(7671):252–256, 2017.
- [21] J. F. Barry, M. J. Turner, J. M. Schloss, D. R. Glenn, Y. Song, D. Lukin, H. Park, and R. L. Walsworth. Optical magnetic detection of single-neuron action potentials using quantum defects in diamond. *Proceedings of the National Academy of Sciences*, 113(49):14133–14138, 2016.
- [22] S. K. Kumar Haldar. *Introduction to Mineralogy and Petrology*. Elsevier, 2014.

- [23] K. Takahashi, A. Yoshikawa, and A. Sandhu. *Wide Bandgap Semiconductors*. Springer, Berlin, Heidelberg, 2007.
- [24] M. A. Prelas, G. Popovici, and I. K. Bigelow, editors. *Handbook of Industrial Diamonds and Diamond Films*. CRC Press, 1998.
- [25] Alexander M. Zaitsev. *Optical Properties of Diamond*. Springer, Berlin, Heidelberg, 2001.
- [26] G. Davies and T. Evans. Graphitization of diamond at zero pressure and at high pressure. *Proc. R. Soc. Lond. A*, 328:413–427, 1972.
- [27] R. S. Balmer, J. R. Brandon, S. L. Clewes, H. K. Dhillon, J. M. Dodson, I. Friel, P. N. Inglis, T. D. Madgwick, M. L. Markham, T. P. Mollart, N. Perkins, G. A. Scarsbrook, D. J. Twitchen, A. J. Whitehead, J. J. Wilman, and S. M. Woollard. Chemical vapour deposition synthetic diamond: materials, technology and applications. *J. Phys.: Condens. Matter*, 21(364221), 2009.
- [28] H. Sumiya and K. Tamasaku. Large defect-free synthetic type iia diamond crystals synthesized via high pressure and high temperature. *Jpn. J. Appl. Phys.*, 51(9R), 2012.
- [29] C. Müller, X. Kong, J.-M. Cai, K. Melentijević, A. Stacey, M. Markham, D. Twitchen, J. Isoya, S. Pezzagna, J. Meijer, J. F. Du, M. B. Plenio, B. Naydenov, L.P. McGuinness, and F. Jelezko. Nuclear magnetic resonance spectroscopy with single spin sensitivity. *Nat. Commun.*, 5(4703), 2014.
- [30] E. Bauch, S. Singh, J. Lee, C. A. Hart, J. M. Schloss, M. J. Turner, J. F. Barry, L. M. Pham, N. Bar-Gill, S. F. Yelin, and R. L. Walsworth. Decoherence of ensembles of nitrogen-vacancy centers in diamond. *Phys. Rev. B*, 102(134210), 2020.

- [31] J. F. Barry, J. M. Schloss, E. Bauch, M. J. Turner, C. A. Hart, L. M. Pham, and R. L. Walsworth. Sensitivity optimization for nv-diamond magnetometry. *Rev. Mod. Phys.*, 92(015004), 2020.
- [32] Richard J. D. Tilley. *Defects in Solids*. John Wiley & Sons, Inc., 2008.
- [33] J. Wrachtrup and F. Jelezko. Processing quantum information in diamond. *J. Phys.: Condens. Matter*, 18(21), 2006.
- [34] F. Jelezko and J. Wrachtrup. Single defect centres in diamond: A review. *Physica Status Solidi (A)*, 203(13):3207–3225, 2006.
- [35] B. Smeltzer, J. McIntyre, and L. Childress. Robust control of individual nuclear spins in diamond. *Phys. Rev. A*, 80(050302), 2009.
- [36] F. Dolde, H. Fedder, M. W. Doherty, T. Nobauer, F. Rempp, G. Balasubramanian, T. Wolf, F. Reinhard, L. C. L. Hollenberg, F. Jelezko, and J. Wrachtrup. Electric-field sensing using single diamond spins. *Nature Physics Letter*, 455:644–647, October 2008.
- [37] V. M. Acosta, E. Bauch, M. P. Ledbetter, A. Waxman, L.-S. Bouchard, and D. Budker. Temperature dependence of the nitrogen-vacancy magnetic resonance in diamond. *Phys. Rev. Lett.*, 104:070801, Feb 2010.
- [38] X. Rong, M. Wang, J. Geng, X. Qin, M. Guo, M. Jiao, Y. Xie, P. Wang, P. Huang, F. Shi, Y.-F. Cai, C. Zou, and J. Du. Searching for an exotic spin-dependent interaction with a single electron-spin quantum sensor. *Nat. Commun.*, 9(739), 2018.
- [39] X. Rong, M. Jiao, J. Geng, B. Zhang, T. Xie, F. Shi, C.-K. Duan, Y.-F. Cai, and J. Du. Constraints on a spin-dependent exotic interaction between electrons with single electron spin quantum sensors. *Phys. Rev. Lett.*, 121(080402), 2018.

- [40] M. Jiao, M. Guo, X. Rong, Y.-F. Cai, and J. Du. Constraint on an exotic parity-odd spin- and velocity-dependent interaction with a single electron spin quantum sensor. *Phys. Rev. Lett.*, 2021.
- [41] J. M. Schloss, J. F. Barry, M. J. Turner, and R. L. Walsworth. Simultaneous broadband vector magnetometry using solid-state spins. *Phys. Rev. Applied*, 10:034044, Sep 2018.
- [42] J. F. Ziegler, M. D. Ziegler, and J. P. Biersack. Srim - the stopping and range of ions in matter (2010). *Nuclear Instruments and Methods in Physics Research Section B: Beam Interactions with Materials and Atoms*, 268(11-12), 2010.
- [43] F. Fávvaro de Oliveira, S. A. Momenzadeh, Y. Wang, M. Konuma, M. Markham, A. M. Edmonds, A. Denisenko, and J. Wrachtrup. Effect of low-damage inductively coupled plasma on shallow nitrogen-vacancy centers in diamond. *Appl. Phys. Lett.*, 107(073107), 2015.
- [44] J. Michl, T. Teraji, S. Zaiser, I. Jakobi G. Waldherr, F. Dolde, P. Neumann, M. W. Doherty, N. B. Manson, J. Isoya, and J. Wrachtrup. Perfect alignment and preferential orientation of nitrogen-vacancy centers during chemical vapor deposition diamond growth on (111) surfaces. *Appl. Phys. Lett.*, 104(102407), 2014.
- [45] M. Lesik, T. Plays, A. Tallaire, J. Achard, O. Brinza, L. William, M. Chipaux, L. Toraille, T. Debuisschert, A. Gicquel, J. F. Roch, and V. Jacques. Preferential orientation of nv defects in cvd diamond films grown on (113)-oriented substrates. *Diamond Relat. Mater.*, 56:47–53, 2015.
- [46] V. M. Acosta, E. Bauch, M. P. Ledbetter, C. Santori, K.-M. Fu, P. E. Barclay, R. G. Beausoleil, H. Linget, J. F. Roch, F. Treussart, S. Chemerisov, W. Gawlik, and D. Budker. Diamonds with a high density of nitrogen-

- vacancy centers for magnetometry applications. *Phys. Rev. B*, 80(115202), 2009.
- [47] C. A. McLellan, B. A. Myers, S. Kraemer, K. Ohno, D. D. Awschalom, and A. C. Bleszynski Jayich. Patterned formation of highly coherent nitrogen-vacancy centers using a focused electron irradiation technique. *Nano Lett.*, 16:2450–2454, 2016.
- [48] K. Ohno, F. Joseph Heremans, C. F. de las Casas, B. A. Myers, B. J. Alemán, A. C. Bleszynski Jayich, and D. D. Awschalom. Three-dimensional localization of spins in diamond using ^{12}C implantation. *Appl. Phys. Lett.*, 105(052406), 2014.
- [49] Z. Huang, W.-D. Li, C. Santori, V. M. Acosta, A. Faraon, T. Ishikawa, W. Wu, D. Winston, R. S. Williams, and R. G. Beausoleil. Diamond nitrogen-vacancy centers created by scanning focused helium ion beam and annealing. *Appl. Phys. Lett.*, 103(081906), 2013.
- [50] Y.-C. Chen, P. S. Salter, S. Knauer, L. Weng, A. C. Frangeskou, C. J. Stephen, S. N. Ishmael, P. R. Dolan S. Johnson, B. L. Green, G. W. Morley, M. E. Newton, J. G. Rarity, M. J. Booth, and J. M. Smith. Laser writing of coherent colour centres in diamond. *Nat. Photonics*, 11:77–80, 2017.
- [51] Ed. E. Kleinsasser, Matthew M. Stanfield, Jannel K. Q. Banks, Zhouyang Zhu, Wen-Di Li, Victor M. Acosta, Hideyuki Watanabe, Kohei M. Itoh, and Kai-Mei C. Fu. High density nitrogen-vacancy sensing surface created via He^+ ion implantation of ^{12}C diamond. *Appl. Phys. Lett.*, 108(202401), 2016.
- [52] S. Pezzagna, B. Naydenoc, F. Jelezko, J. Wrachtrup, and J. Meijer. Creation efficiency of nitrogen-vacancy centres in diamond. *New J. Phys.*, 12(065017):065017, 2010.

- [53] T. Lühmann, N. Raatz, R. John, M. Lesik, J. Rödiger, M. Portail, D. Wildanger, F. Kleiβler, K. Nordlund, A. Zaitsev, J.-F. Roche, A. Tal-laire, J. Meijer, and S. Pezzagna. Screening and engineering of colour centres in diamond. *J. Phys. D: Appl. Phys.*, 51(48), 2018.
- [54] C. Kucsko, S. Choi, P. C. Maurer, H. Zhou, R. Landig, H. Sumiya, S. On-oda, J. Isoya, F. Jelezko, E. Demler, N. Y. Yao, and M. D. Lukin. Critical thermalization of a disordered dipolar spin system in diamond. *Phys. Rev. Lett.*, 121(023601), 2018.
- [55] J. M. Smith, S. A. Meynell, A. C. Bleszynski Jayich, and J. Meijer. Colour centre generation in diamond for quantum technologies. *Nanophotonics*, 8(11):1889–1906, 2019.
- [56] M. W. Doherty, N. B. Manson, P. Delaney, F. Jelezko, J. Wrachtrup, and L. C.L. Hollenberg. The nitrogen-vacancy colour centre in diamond. *Phys. Rep.*, 528:1–45, 2013.
- [57] V. M. Acosta, A. Jarmola, E. Bauch, and D. Budker. Optical properties of the nitrogen-vacancy singlet levels in diamond. *Phys. Rev. B*, 82(201202), 2010.
- [58] Victor M. Acosta. *Optical Magnetometry with Nitrogen-Vacancy Centers in Diamond*. Dissertation, University of California, Berkeley, 2011.
- [59] Y. Dumeige, M. Chipaux, V. Jacques, F. Treussart, J.-F. Roch, T. De-buisschert, V. M. Acosta, A. Jarmola, K. Jensen, P. Kehayias, and D. Bud-ker. Magnetometry with nitrogen-vacancy ensembles in diamond based on infrared absorption in a doubly resonant optical cavity. *Phys. Rev. B*, 87(155202), 2013.
- [60] J. Kölbl, M. Kasperczyk, B. Bürgler, A. Barfuss, and P. Maletinsky. Deter-mination of intrinsic effective fields and microwave polarizations by high-resolution spectroscopy of single nitrogen-vacancy center spins. *New Jour-nal of Physics*, 21(113039), 2019.

- [61] S. Felton, A. M. Edmonds, M. E. Newton, P. M. Martineau, D. Fisher, D. J. Twitchen, and J. M. Baker. Hyperfine interaction in the ground state of the negatively charged nitrogen vacancy center in diamond. *Physical Review B*, 79(075203), 2009.
- [62] J. R. Rabeau and P. Reichart. Implantation of labelled single nitrogen vacancy centers in diamond using ^{15}n . *Appl. Phys. Lett.*, 88(023113), 2006.
- [63] M. Lesik, J.-P. Tetienne, A. Tallaire, J. Achard, V. Mille, A. Gicquel, J.-F. Roch, and V. Jacques. Perfect preferential orientation of nitrogen-vacancy defects in a synthetic diamond sample. *Appl. Phys. Lett.*, 104:113107, 2014.
- [64] L. Rondin, J.-P. Tetienne, T. Hingant, J.-F. Roch, P. Maletinsky, and V. Jacques. Magnetometry with nitrogen-vacancy defects in diamond. *Rep. Prog. Phys.*, 77(5):056503, may 2014.
- [65] N. Hedrich, D. Rohner, M. Batzer, P. Maletinsky, and B. J. Shields. Parabolic diamond scanning probes for single-spin magnetic field imaging. *Phys. Rev. Applied*, 14(064007), 2020.
- [66] Peter van der Straten and Harold Metcalf. *Atoms and Molecules Interacting with Light: Atomic Physics for the Laser Era*. Cambridge University Press, 2016.
- [67] Marlan O. Scully and M. Suhail Zubairy. *Quantum Optics*. Cambridge University Press, 1997.
- [68] P. W. Milonni and J. H. Eberky. *Laser Physics*. John Wiley & Sons, Ltd, 2010.
- [69] M. Auzinsh, D. Budker, and S. Rochester. *Optically polarized atoms: understanding light-atom interactions*. Oxford University Press, 2010.
- [70] A. Dréau, M. Lesik, L. Rondin, P. Spinicelli, O. Arcizit, J.-F. Roch, and V. Jacques. Avoiding power broadening in optically detected magnetic

- resonance of single nv defects for enhanced dc magnetic field sensitivity. *Phys. Rev. B*, 84(195204), 2011.
- [71] Norman F. Ramsey. A molecular beam resonance method with separated oscillating fields. *Phys. Rev.*, 78(695), 1950.
- [72] B. Naydenov, F. Dolde, L. T. Hall, C. Shin, H. Fedder, L. C. L. Hollenberg, F. Jelezko, and J. Wrachtrup. Dynamical decoupling of a single-electron spin at room temperature. *Phys. Rev. B*, 83(081201), 2011.
- [73] C. A. Ryan, J. S. Hodges, and D. G. Cory. Robust decoupling techniques to extend quantum coherence in diamond. *Phys. Rev. Lett.*, 105(200402), 2010.
- [74] L. M. Pham, S. J. DeVience, F. Casola, I. Lovchinsky, A. O. Sushkov, E. Bersin, J. Lee, E. Urbach, P. Cappellaro, H. Park, A. Yacoby, M. Lukin, and R. L. Walsworth. NMR technique for determining the depth of shallow nitrogen-vacancy centers in diamond. *Phys. Rev. B*, 93:045425, Jan 2016.
- [75] L. Emban, Y. Anahory, A. Suhov, D. Halbertal, J. Cuppens, A. Yakovenko, A. Uri, Y. Myasoedov, M. L. Rappaport, M. E. Huber, A. Gurevich, and E. Zeldov. Probing dynamics and pinning of single vortices in superconductors at nanometer scales. *Sci. Rep.*, 5:7598, 2015.
- [76] B. Kalisky, J. R. Kirtley, J. G. Analytis, Jiun-Haw Chu, A. Vailionis, I. R. Fisher, and K. A. Moler. Stripes of increased diamagnetic susceptibility in underdoped superconducting $\text{Ba}(\text{Fe}_{1-x}\text{Co}_x)_2\text{As}_2$ single crystals: Evidence for an enhanced superfluid density at twin boundaries. *Phys. Rev. B*, 81(184513):184513, 2010.
- [77] L. Embon, Y. Anahory, Ž. L. Jelić, E. O. Lachman, Y. Myasoedov, M. E. Huber, G.P. Mikitik, A. V. Silhanek, M. V. Milošević, A. Gurevich, and E. Zeldov. Imaging of super-fast dynamics and flow instabilities of superconducting vortices. *Nat. Commun.*, 8(85):85, 2017.

- [78] A. Kremen, S. Wissberg, N. Haham, E. Persky, Y. Frenkel, and B. Kalisky. Mechanical control of individual superconducting vortices. *Nano Lett.*, 16:1626, 2016.
- [79] B. Raes, J. Van de Vondel, A. V. Silhanek, C. C. de Souza Silva, J. Gutierrez, R. B. G. Kramer, and V. V. Moshchalkov. Local mapping of dissipative vortex motion. *Phys. Rev. B*, 86(064522):064522, 2012.
- [80] D. Cole, S. Bending, S. Sael'ev, A. Grigorenko, T. Tamegai, and F. Nori. Ratchet without spatial asymmetry for controlling the motion of magnetic flux quanta using time-asymmetric drives. *Nat. Mater.*, 5:305, 2006.
- [81] A. M. Chang, H. D. Hallen, H. F. Hess and H. L. Kao, J. Kwo, A. Sudbø, and T. Y. Chang. Scanning hall-probe microscopy of a vortex and field fluctuations in $\text{L}_{1.85}\text{Sr}_{0.15}\text{CuO}_0$ films. *Europhys. Lett.*, 20:645, 1992.
- [82] I. V. Grigorieva. Magnetic flux decoration of type-II superconductors. *Supercond. Sci. Technol.*, 7(161):161, 1994.
- [83] S. Rablen, M. Kemmler, T. Quaglio, R. Kleiner, D. Koelle, and I. V. Grigorieva. Bitter decoration of vortex patterns in superconducting Nb films with random, triangular, and penrose arrays of antidots. *Phys Rev B*, 84(184520):184520, 2011.
- [84] Y. Fasano, M. De Seta, M. Menghini, H. Pastoriza, and F. de la Cruz. Comensurability and stability in nonperiodic systems. *Proc Natl Acad Sci U S A*, 102:3898, 2005.
- [85] J. A. Xia, N. J. Long, N.M. Strickland, P. Hoefakker, E. F. Talantsev, X. Li, W. Zhang, T. Kodenkandath, Y. Huang, and M. W. Rupich. Tem observation of the microstructure of metal-organic deposited $\text{YBa}_2\text{Cu}_3\text{O}_{x-\delta}$ with Dy additions. *Supercond. Sci. Technol.*, 20:8, 2007.
- [86] J. C. Loudon, S. Yazdi, T. Kasama, N. D. Zhigadlo, and J. Karpinski. Measurement of the penetration depth and coherence length of MgB_2 in all di-

- reactions using transmission electron microscopy. *Phys. Rev. B*, 91:054505, 2015.
- [87] Ø. Fischer, M. Kugler, I. Maggio-Aprile, C. Berthod, and C. Renner. Scanning tunneling spectroscopy of high-temperature superconductors. *Rev. Mod. Phys.*, 79:353, 2007.
- [88] Ken Harada. Lorentz microscopy observation of vortices in high- T_c superconductors using a 1 MV field emission transmission microscope. *Microscopy*, 62:S3, 2013.
- [89] P. E. Goa, H. Hauglin, M. Baziljevich, E. Il'yachenko, P. L Gammel, and Tom. H Johansen. Real-time magneto-optical imaging of vortices in superconducting NbSe₂. *Supercond. Sci. Technol.*, 14:729, 2001.
- [90] Simon J. Bending. Local magnetic probes of superconductors. *Adv. Phys.*, 48(4):449, 1999.
- [91] L.-S. Bouchard, V. M. Acosta, E. Bauch, and D. Budker. Detection of the Meissner effect with a diamond magnetometer. *New J. Phys.*, 13(025017):025017, 2011.
- [92] A. Horsley, P. Appel, J. Wolters, J. Achard, A. Tallaire, P. Maletinsky, and P. Treutlein. Microwave device characterisation using a widefield diamond microscope. *Phys. Rev. Applied*, 10(044039), 2018.
- [93] V. M. Acosta, E. Bauch, M. P. Ledbetter, A. Waxman, L.-S. Bouchard, and D. Budker. Temperature dependence of the nitrogen-vacancy magnetic resonance in diamond. *Phys. Rev. Lett.*, 104:070801, Feb 2010.
- [94] V. M. Acosta, E. Bauch, A. Jarmola, L. J. Zipp, M. P. Ledbetter, and D. Budker. Broadband magnetometry by infrared-absorption detection of nitrogen-vacancy ensembles in diamond. *Appl. Phys. Lett.*, 97:174104, 2010.

- [95] K. Jensen, P. Kehayias, and D. Budker. *High Sensitivity Magnetometers*, chapter Magnetometry with Nitrogen-Vacancy Centers in Diamond, pages 553–576. Springer International Publishing, 2017.
- [96] M. W. Doherty, F. Dolde, H. Fedder, F. Jelezko, J. Wrachtrup, N. B. Manson, and L. C. L. Hollenberg. Theory of the ground-state spin of the NV⁻ center in diamond. *Phys. Rev. B*, 85(205203):205203, 2012.
- [97] Gilson Carneiro and Ernst Helmut Brandt. Vortex lines in films: Fields and interactions. *Phys. Rev. B*, 61:6370, 2000.
- [98] G. Blatter, M. V. Feigel'man, V. B. Geshkenbein, A. I. Larkin, and V. M. Vinokur. Vortices in high-temperature superconductors. *Rev. Mod. Phys.*, 66:1125, 1994.
- [99] C. S. Shin, C. E. Avalor, M. C. Butler, D. R. Trease, S. J. Seltzer, J. P. Mustonen, D. J. Kennedy, V. M. Acosta, D. Budker, A. Pines, and V. S. Bajaj. Room temperature operation of a radiofrequency diamond magnetometer near the shot noise limit. *J. Appl. Phys.*, 112:124519, 2012.
- [100] N. Aslam, M. Pfender, P. Neumann, R. Reuter, A. Zappe, F. Fávoro de Oliveira, A. Denisenko, H. Sumiya, S. Onoda, J. Isoya, and J. Wrachtrup. Nanoscale nuclear magnetic resonance with chemical resolution. *Science*, 357(6346):67, 2017.
- [101] P. Appel, E. Neu, M. Ganzhorn, A. Barfuss, M. Batzer, M. Gratz, A. Tschöpe, and P. Maletinsky. Fabrication of all diamond scanning probes for nanoscale magnetometry. *Rev. Sci. Instrum.*, 87(063703):063703, 2016.
- [102] D. Riedel, D. Rohner, M. Ganzhorn, T. Kaldewey, P. Appel, E. Neu, R. J. Warburton, and P. Maletinsky. Low-loss broadband antenna for efficient photon collection from a coherent spin in diamond. *Phys. Rev. Appl.*, 2:064011, 2014.

- [103] R. L. Stamps, S. Breitzkreutz, J. Åkerman, A. V. Chumak, Y. Otani, G. E. W. Bauer, J.-U. Thiele, M. Bowen, S. A. Majetich, M. Kläui, I. L. Prejbeanu, B. Dieny, N. M. Dempsey, and B. Hillebrands. The 2014 magnetism roadmap. *J. Phys. D: Appl. Phys.*, 47(33):333001, jul 2014.
- [104] D. Sander, S. O. Valenzuela, D. Makarov, C. H. Marrows, E. E. Fullerton, P. Fischer, J. McCord, P. Vavassori, S Mangin, P Pirro, B Hillebrands, A D Kent, T Jungwirth, O Gutfleisch, C G Kim, and A Berger. The 2017 magnetism roadmap. *Journal of Physics D: Applied Physics*, 50(36):363001, aug 2017.
- [105] F. El Gabaly, S. Gallego, C. Muñoz, L. Szunyogh, P. Weinberger, C. Klein, A. K. Schmid, K. F. McCarty, and J. de la Figuera. Imaging spin-reorientation transitions in consecutive atomic co layers on ru(0001). *Phys. Rev. Lett.*, 96:147202, Apr 2006.
- [106] N. Rougemaille and A. K. Schmid. Magnetic imaging with spin-polarized low-energy electron microscopy. *Eur. Phys. J. Appl. Phys.*, 50(2):20101, 2010.
- [107] Peter Fischer. Magnetic imaging with polarized soft x-rays. *Journal of Physics D: Applied Physics*, 50(31):313002, jul 2017.
- [108] Stefano Bonetti. X-ray imaging of spin currents and magnetisation dynamics at the nanoscale. *Journal of Physics: Condensed Matter*, 29(13):133004, feb 2017.
- [109] J. A. Slides, J. L. Garbini, K. J. Bruland, D. Rugar, O. Züger, S. Hoen, and C. S. Yannoni. Magnetic resonance force microscopy. *Rev. Mod. Phys.*, 67(249), 1995.
- [110] I. Lee, Y. Obukhov, G. Xiang, A. Hauser, F. Yang, P. Banerjee, D. V. Pelekhov, and P. C. Hammel. Nanoscale scanning probe ferromagnetic resonance imaging using localized modes. *Nature*, 466(7308):845–848, 2010.

- [111] John R. Kirtley and Jr. John P Wikswo. Scanning squid microscopy. *Annu. Rev. Mater. Sci.*, 1999.
- [112] D. Vasyukov, Y. Anahory, L. Embon, D. Halbertal, J. Cuppens, L. Neeman, A. Finkler, Y. Segev, Y. Myasoedov, M. L. Rappaport, M. E. Huber, and E. Zeldov. A scanning superconducting quantum interference device with single electron spin sensitivity. *Nature Nanotechnology*, 8(9):639–644, 2013.
- [113] Francesco Casola, Toeno van der Sar, and Amir Yacoby. Probing condensed matter physics with magnetometry based on nitrogen-vacancy centres in diamond. *Nature Reviews Materials*, 3(1):17088, 2018.
- [114] J.-P. Tetienne, T. Hingant, J.-V. Kim, L. Herrera Diez, J.-P. Adam, K. Garcia, J.-F. Roch, S. Rohart, A. Thiaville, D. Ravelosona, and V. Jacques. Nanoscale imaging and control of domain-wall hopping with a nitrogen-vacancy center microscope. *Science*, 344(6190):1366–1369, 2014.
- [115] I. Gross, L. J. Martínez, J.-P. Tetienne, T. Hingant, J.-F. Roch, K. Garcia, R. Soucaille, J. P. Adam, J.-V. Kim, S. Rohart, A. Thiaville, J. Torreon, M. Hayashi, and V. Jacques. Direct measurement of interfacial dzyaloshinskii-moriya interaction in x |CoFeB|MgO heterostructures with a scanning nv magnetometer ($x = \text{Ta}, \text{TaN}, \text{and W}$). *Phys. Rev. B*, 94:064413, Aug 2016.
- [116] I. Gross, W. Akhtar, A. Hrabec, J. Sampaio, L. J. Martínez, S. Chouaieb, B. J. Shields, P. Maletinsky, A. Thiaville, S. Rohart, and V. Jacques. Skyrmion morphology in ultrathin magnetic films. *Phys. Rev. Materials*, 2:024406, Feb 2018.
- [117] Alec. Jenkins, M. Pelliccione, G. Yu, X. Ma, X. Li, K. L. Wang, and A. C. B. Jayich. Single-spin sensing of domain-wall structure and dynamics in a thin-film skyrmion host. *Phys. Rev. Materials*, 3:083801, Aug 2019.

- [118] M. Chipaux, A. Tallaire, J. Achard, S. Pezzagna, J. Meijer, V. Jacques, J.-F. Roch, and T. Debuisschert. Magnetic imaging with an ensemble of nitrogen-vacancy centers in diamond. *The European Physical Journal D5*, 69(7):166, 2015.
- [119] D. R. Glenn, K. Lee, H. Park, R. Weissleder, A. Yacoby, M. D. Lukin, H. Lee, R. L. Walsworth, and C. B. Connolly. Single-cell magnetic imaging using a quantum diamond microscope. *Nature Methods*, 12(8):736–738, 2015.
- [120] I. Fescenko, A. Laraoui, J. Smits, N. Mosavian, P. Kehayias, J. Seto, L. Bougas, A. Jarmola, and V. M. Acosta. Diamond magnetic microscopy of malarial hemozoin nanocrystals. *Phys. Rev. Applied*, 11:034029, Mar 2019.
- [121] Y. Dovzhenko, F. Casola, S. Schlotter, T. X. Zhou, F. Büttner, R. L. Walsworth, G. S. D. Beach, and A. Yacoby. Magnetostatic twists in room-temperature skyrmions explored by nitrogen-vacancy center spin texture reconstruction. *Nature Communications*, 9(2712), 2018.
- [122] A. Y. Meltzer, E. Levin, and E. Zeldov. Direct reconstruction of two-dimensional currents in thin films from magnetic-field measurements. *Phys. Rev. Applied*, 8:064030, Dec 2017.
- [123] Jeffrey McCord. Progress in magnetic domain observation by advanced magneto-optical microscopy. *Journal of Physics D: Applied Physics*, 48(33):333001, jul 2015.
- [124] E Bourgeois, A Jarmola, P Siyushev, M Gulka, J Hruby, F Jelezko, D Budker, and M Nesladek. Photoelectric detection of electron spin resonance of nitrogen-vacancy centres in diamond. *Nature Communications*, 6(1):8577, 2015.
- [125] S. Steinert, F. Dolde, P. Neumann, A. Aird, B. Naydenov, G. Balasubramanian, F. Jelezko, and J. Wrachtrup. High sensitivity magnetic imaging

using an array of spins in diamond. *Review of Scientific Instruments*, 81(4):043705, 2010.

- [126] D. Le Sage, K. Arai, D. R. Glenn, S. J. DeVience, L. M. Pham, L. Rhan-Lee, M. D. Lukin, A. Yacobi, A. Komeili, and R. L. Walsworth. Optical imaging of living cells. *Nature*, 496:486, 2013.
- [127] Y. Schlüssel, T. Lenz, D. Rohner, Y. Bar-Haim, L. Bougas, D. Groswasser, M. Kieschnick, E. Rozenberg, L. Thiel, A. Waxman, J. Meijer, P. Maletinsky, D. Budker, and R. Folman. Wide-field imaging of superconductor vortices with electron spins in diamond. *Phys. Rev. Appl*, 10(034032), 2018.
- [128] A. Nowodzinski, M. Chipaux, L Toraille, V. Jacques, J.-F. Roch, and T. Debuisschert. Nitrogen-vacancy centers in diamond for current imaging at the redistributive layer level of integrated circuits. *Microelectron. Reliab.*, 55:1549–1553, 2015.
- [129] S. E. Lillie, N. Dontschuk, D. A. Broadway, D. L. Creedon, L. C. L. Hollenberg, and J.-P. Tetienne. Imaging graphene field-effect transistors on diamond using nitrogen-vacancy microscopy. *Phys. Rev. Appl.*, 12(024018), 2019.
- [130] J. Zázvorka, F. Jakobs, D. Heinze, N. Keil, S. Kromin, S. Jaiswal, K. Litzius, G. Jakob, P. Virnau, D. Pinna, K. Everschor-Sitte, L. Rózsa, A. Donges, U. Nowak, and M. Kläui. Thermal skyrmion diffusion used in a reshuffler device. *Nature Nanotechnology*, 14(7):658–661, 2019.
- [131] G. Yu, P. Upadhyaya, X. Li, W. Lu, S. Kwon Kim, K. L. Wong, Y. Tserkovnyak, P. Khalili Amiri, and K. L. Wang. Room-temperature creation and spin-orbit torque manipulation of skyrmions in thin films with engineered asymmetry. *Nano Lett.*, 16(3):1981, 2016.
- [132] B.-F. Miao, Y.-T. Millev, L. Sun, B. You, W. Zhang, and H.-F. Ding.

- Thickness-driven spin reorientation transition in ultrathin films. *Sci. China Phys. Mech. Astron.*, 56, 2013.
- [133] I. Lemesh, K. Litzius, M. Böttcher, P. Bassirian, N. Kerber, D. Heinze, J. Zázvorka, F. Büttner, L. Caretta, M. Mann, M. Weigand, S. Finizio, J. Raabe, M.-Y. Im, H. Stoll, G. Schütz, B. Dupé, M. Kläui, and G. S. D. Beach. Current-induced skyrmion generation through morphological thermal transitions in chiral ferromagnetic heterostructures. *Adv. Mater.*, 30(49), 2018.
- [134] J. F. Barry, M. J. Turner, J. M. Schloss, D. R. Glenn, Y. Song, M. D. Lukin, H. Park, and R. L. Walsworth. Optical magnetic detection of single-neuron action potentials using quantum defects in diamond. *Proceedings of the National Academy of Sciences*, 113(49):14133–14138, 2016.
- [135] I. Lovchinsky, J. D. Sanchez-Yamagishi, E. K. Urbach, S. Choi, S. Fang, T. I. Andersen, K. Watanabe, T. Taniguchi, A. Bylinskii, E. Kaxiras, P. Kim, H. Park, and M. D. Lukin. Magnetic resonance spectroscopy of an atomically thin material using a single-spin qubit. *Science*, 355(6324):503–507, 2017.
- [136] H. Zheng, J. Xu, G. Z. Iwata, T. Lenz, J. Michl, B. Yavkin, K. Nakamura, H. Sumiya, T. Ohshima, J. Wrachtrup, A. Wickenbrock, and D. Budker. Zero-field magnetometry based on nitrogen-vacancy ensembles in diamond. *Phys. Rev. Appl*, 11(064068), 2019.
- [137] Huijie Zheng, Zhiyin Sun, Georgios Chatzidrosos, Chen Zhang, Kazuo Nakamura, Hitoshi Sumiya, Takeshi Ohshima, Junichi Isoya, Jörg Wrachtrup, Arne Wickenbrock, and Dmitry Budker. Microwave-free vector magnetometry with nitrogen-vacancy centers along a single axis in diamond. *Phys. Rev. Appl*, 13(044023), 2020.
- [138] A. Wickenbrock, H. Zheng, L. Bougas, N. Leefer, S. Afach, A. Jarmola,

- V. M. Acosta, and D. Budker. Microwave-free magnetometry with nitrogen-vacancy centers in diamond. *Appl. Phys. Lett.*, 109(053505), 2016.
- [139] M. Mrózek, J. Mlynarczyk, D. S. Rudnicki, and W. Gawlik. Circularly polarized microwaves for magnetic resonance study in the ghz range: Application to nitrogen-vacancy in diamonds. *Appl. Phys. Lett.*, 107(013505), 2015.
- [140] I. Lovchinsky, A. O. Sushkov, E. Urbach, N. P. de Leon, S. Choi, K. De Greve, R. Evans, R. Gertner, E. Bersin, C. Müller, L. McGuinness, F. Jelezko, R. L. Walsworth, H. Park, and M. D. Lukin. Nuclear magnetic resonance detection and spectroscopy of single proteins using quantum logic. *Science*, 351:836–841, 2016.
- [141] X. Rong, M. Jiao, M. Guo, D. Wu, and J. Du. Observation of a new interaction between a single spin and a moving mass. *arXiv:2010.15667*, 2020.
- [142] John W. Blanchard and Dmitry Budker. Zero- to ultralow-field nmr. *eMagRes*, 5(3), 2016.
- [143] J. Zázvorka, F. Dittrich, Y. Ge, N. Kerber, K. Raab, T. Winkler, K. Litzius, M. Veis, P. Virnau, and M. Kläui. Skyrmion lattice phases in thin film multilayer. *arXiv:2004.09244*, 2020.
- [144] T. P. Mayer Alegre, C. Santori, G. Medeiros-Ribeiro, and R. G. Beausoleil. Polarization-selective excitation of nitrogen vacancy centers in diamond. *Phys. Rev. B*, 76(165205), 2007.
- [145] D. R. Glenn, R. R. Fu, P. Kehayias, D. Le Sage, E. A. Lima, B. P. Weiss, and R. L. Walsworth. Micrometer-scale magnetic imaging of geological samples using a quantum diamond microscope. *Geochem., Geophys., Geosyst.*, 18:3254, 2017.

- [146] M. Steiner, P. Neumann, J. Beck, F. Jelezko, and J. Wrachtrup. Universal enhancement of the optical readout fidelity of single electron spins at nitrogen-vacancy centers in diamond. *Phys. Rev. B*, 81(035205), 2010.
- [147] P. Neumann, J. Beck, M. Steiner, F. Rempp, H. Fedder, P. R. Hemmer, J. Wrachtrup, and F. Jelezko. Single-shot readout of a single nuclear spin. *Science*, 329(5991), 2010.
- [148] T. Mittiga, S. Hsieh, C. Zu, B. Kobrin, F. Machado, P. Bhattacharyya, N. Z. Rui, A. Jarmola, S. Choi, D. Budker, and N. Y. Yao. Imaging the local charge environment of nitrogen-vacancy centers in diamond. *Phys. Rev. Lett.*, 121(246402), 2018.
- [149] D. Pagliero, A. Laraoui, J. D. Henshaw, and C. A. Meriles. Recursive polarization of nuclear spins in diamond at arbitrary magnetic fields. *Appl. Phys. Lett.*, 2014.
- [150] A. K. Vershovskii and A. K. Dmitriev. A weak magnetic field sensor based on nitrogen-vacancy color centers in a diamond crystal. *Technical Physics*, 65:1301, 2020.
- [151] S. Schmitt, T. Gefen, F. M. Stürmer, T. Unden, G. Wolff, C. Müller, J. Scheuer, B. Naydenov, M. Markham, S. Pezzagna, J. Meijer, I. Schwarz, M. Plenio, A. Retzker, L. P. McGuinness, and F. Jelezko. Submillihertz magnetic spectroscopy performed with a nanoscale quantum sensor. *Science*, 356(6340):832–837, 2017.
- [152] D. R. Glenn, D. B. Bucher, J. Lee, M. D. Lukin, H. Park, and R. L. Waksforth. High-resolution magnetic resonance spectroscopy using a solid-state spin sensor. *Nature*, 555:351–354, 2018.
- [153] Dmitry Budker. Extreme nuclear magnetic resonance: Zero field, single spins, dark matter... *J Magn Reson*, 306:66, 2019.